

RESEARCH ARTICLE

10.1002/2015JE004874

Key Points:

- Diviner data of previously identified olivine-enriched regions on the lunar surface are examined
- Olivine enriched, pyroxene poor regions of the moon exhibit a wide compositional range
- Linear spectral mixing may not be applicable to lunar regolith-sized grains in the mid-IR

Supporting Information:

- Supporting Information S1

Correspondence to:

J. A. Arnold,
jessica.arnold@physics.ox.ac.uk

Citation:

Arnold, J. A., T. D. Glotch, P. G. Lucey, E. Song, I. R. Thomas, N. E. Bowles, and B. T. Greenhagen (2016), Constraints on olivine-rich rock types on the Moon as observed by Diviner and M³: Implications for the formation of the lunar crust, *J. Geophys. Res. Planets*, 121, doi:10.1002/2015JE004874.

Received 17 JUN 2015

Accepted 21 JUN 2016

Accepted article online 26 JUN 2016

Constraints on olivine-rich rock types on the Moon as observed by Diviner and M³: Implications for the formation of the lunar crust

J. A. Arnold^{1,2}, T. D. Glotch¹, P. G. Lucey³, E. Song⁴, I. R. Thomas^{2,5}, N. E. Bowles², and B. T. Greenhagen⁶

¹Department of Geosciences, Stony Brook University, Stony Brook, New York, USA, ²Atmospheric, Oceanic and Planetary Physics, Department of Physics, Oxford University, Oxford, UK, ³Hawaii Institute of Geophysics and Planetology, University of Hawaii, Honolulu, Hawaii, USA, ⁴Jet Propulsion Laboratory, Pasadena, California, USA, ⁵Royal Belgian Institute for Space Aeronomy, Brussels, Belgium, ⁶The Johns Hopkins University Applied Physics Laboratory, Laurel, Maryland, USA

Abstract We place upper limits on lunar olivine abundance using midinfrared (5–25 μm) data from the Lunar Reconnaissance Orbiter Diviner Lunar Radiometer Experiment (Diviner) along with effective emissivity spectra of mineral mixtures in a simulated lunar environment. Olivine-bearing, pyroxene-poor lithologies have been identified on the lunar surface with visible-near-infrared (VNIR) observations. Since the Kaguya Spectral Profiler (SP) VNIR survey of olivine-rich regions is the most complete to date, we focus this work on exposures identified by that study. We first confirmed the locations with VNIR data from the Moon Mineralogy Mapper (M³) instrument. We then developed a Diviner olivine index from our laboratory data which, along with M³ and Lunar Reconnaissance Orbiter Camera wide-angle camera data, was used to select the geographic area over which Diviner emissivity data were extracted. We calculate upper limits on olivine abundance for these areas using laboratory emissivity spectra of anorthite-forsterite mixtures acquired under lunar-like conditions. We find that these exposures have widely varying olivine content. In addition, after applying an albedo-based space weathering correction to the Diviner data, we find that none of the areas are unambiguously consistent with concentrations of forsterite exceeding 90 wt %, in contrast to the higher abundance estimates derived from VNIR data.

1. Introduction

Locations on the Moon with olivine-bearing, pyroxene-poor lithologies have been detected with both telescopic [Pieters, 1982; Lucey et al., 1986, 1991] and orbital visible-near-infrared (VNIR, roughly 0.4 μm –2.5 μm) observations from instruments such as the Clementine ultraviolet-visible spectroscopy camera [Tompkins and Pieters, 1999], the Chandrayaan-1 Moon Mineralogy Mapper (M³) [Pieters et al., 2009; Mustard et al., 2011; Powell et al., 2012], and the Kaguya (SELENE) Spectral Profiler (SP) [Yamamoto et al., 2010, 2012]. Prior to SP and M³ observations, olivine-bearing exposures had been identified in only a handful of areas including the central peak and walls of Copernicus and ejecta of Aristarchus craters [Pieters, 1982; Lucey et al., 1986, 1991; Tompkins and Pieters, 1999]. Now there are data of sufficient spatial and spectral coverage and resolution to show that olivine-bearing lithologies are concentrated near the edges of large impact basins, mostly within the ejecta, walls, and central peaks of impact craters [Yamamoto et al., 2010, 2012; Dhingra et al., 2011; Powell et al., 2012; Kramer et al., 2013]. In addition to the distribution of these lithologies, the relative abundances of olivine and plagioclase, along with olivine chemistry, can help distinguish among hypotheses for the formation of this material. Extensive exposures of dunite (a rock type containing >90% olivine) would be indicative of overturned mantle material. Lower concentrations of olivine consistent with trocolite (40%–90% olivine) could represent exposures of either the crust-mantle interface or mafic plutons that have intruded into the anorthositic crust. In the latter case, a wide variety of olivine chemistries would be expected.

Previous mineral abundance estimates of olivine-rich locations were derived from VNIR data. Data from VNIR instruments are useful for pinpointing areas where olivine is the dominant mafic component. However, because plagioclase is spectroscopically transparent at these wavelengths, relative abundances of mafics and plagioclase derived from VNIR data are less certain unless the abundance of plagioclase is very high (≥ 90 vol%) [Sunshine et al., 1990; Serventi et al., 2013; Cheek and Pieters, 2014], and spectral mixing is strongly nonlinear in the VNIR. Moreover, olivine, pyroxene, and plagioclase all have overlapping bands in the 1–1.3 μm wavelength region (Figure 1).

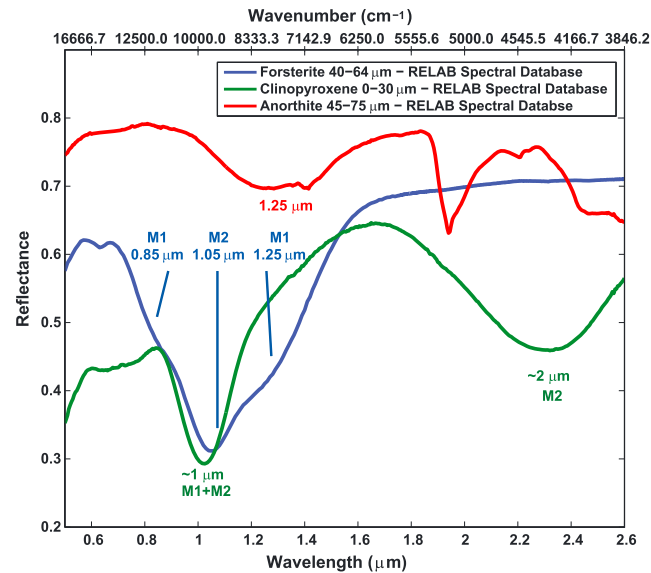


Figure 1. Laboratory bidirectional VNIR reflectance spectra of forsterite, clinopyroxene, and anorthite. Note that the 1.9 μm and smaller 2.2 μm features in the Anorthite samples are due to clay impurities. Relab sample numbers: forsterite (DH-MBW-008/BKR1DH008); anorthite (PA-CMP-060-C/C3PA60); and clinopyroxene (RB-JFM-045-CPX/C1RB45CPX).

Olivine is identified at VNIR wavelengths by three overlapping Fe^{2+} bands near 1.1 μm whose positions shift slightly with composition or Fo# ($=100 \times \text{MgO}/(\text{MgO} + \text{FeO}_i)$) [Sunshine and Pieters, 1998; Dyar et al., 2009; Isaacson et al., 2014]. Pyroxene exhibits two sets of Fe^{2+} bands: one shortward of 1 μm , centered near 0.9 μm for low-Ca pyroxene and shifting to longer wavelengths with increasing Ca content [Adams and McCord, 1972; Klima et al., 2008, 2011], and one at 2 μm . Crystalline plagioclase has a weak absorption feature ($\sim 5\text{--}10\%$ contrast in reflectance) that ranges from 1.1 μm albite of An_2 at the shortward end to 1.3 μm for bytownite of An_{79} at the longward end and an intermediate value of roughly 1.25 μm for anorthite of An_{97} [Adams and Goullaud, 1978]. In lunar samples, this is primarily due to substitution of small amounts of Fe^{2+} for Ca^{2+} [Pieters, 1996]. The plagioclase absorption is masked in mixtures with

mafic by deep absorption features, even for small amounts of olivine or pyroxene [Nash and Conel, 1974; Crown and Pieters, 1987; Klima et al., 2008; Isaacson et al., 2011]. The 1 μm band of pyroxene diminishes the relative strength of the 1.25 μm band of plagioclase after the addition of only a few weight percent pyroxene [e.g., Ohtake et al., 2009]. However, the addition of pyroxene to plagioclase produces substantial changes to the pyroxene spectrum with <10 vol% pyroxene in the mixture, whereas admixture of less than 10 vol% olivine masks plagioclase [Cheek and Pieters, 2014]. Additionally, the Fe^{2+} absorption is affected by amorphization due to shock [Adams et al., 1979], resulting in a weaker 1.2–1.3 μm band and a shift in the main absorption feature toward 1 μm [Pieters, 1996; Johnson and Hörz, 2003]. Although estimates of plagioclase, pyroxene, and olivine abundances can be derived from VNIR spectra through nonlinear spectral unmixing (typically using the Hapke [1981, 1993]—or Shkuratov et al. [1999]—based implementations of radiative transfer theory [e.g., Tompkins and Pieters, 1999; Cahill et al., 2010]), Cahill et al. [2010] found that plagioclase abundance is typically underestimated, while no single phase is correspondingly overestimated.

Yamamoto et al. [2010] Supporting Online Material (SOM) fit SP spectra (0.5–2.6 μm) for 6 out of 33 total regional detections with a radiative transfer-based intimate mixture model [Denevi et al., 2008]. The components in this model included Fo_{90} crystalline olivine, crystalline orthopyroxene ($\text{Fe}_{15}\text{Mg}_{85}\text{Ca}_0$), and an agglutinate component with the same chemical composition as the olivine and orthopyroxene components. Even with this dark agglutinate component, Yamamoto et al. [2010] reported some difficulties matching the abundance of plagioclase without overestimating the albedo of lunar soil. For the six sites where mineral abundances were estimated, the range of abundances reported for these three components is as follows: 45.3%–76.8 wt% crystalline olivine, 2.3%–7.8 wt% crystalline orthopyroxene, and 16.4%–46.9 wt% agglutinate. Summing the amount of crystalline olivine with the portion of agglutinate that has olivine chemistry, the lowest total olivine content is placed at 85%, while the highest is 97%.

Unlike the VNIR, the midinfrared (MIR, roughly 5–25 μm) is sensitive to SiO_2 content and structure via the wavelength position of an emissivity maximum near 7–9 μm known as the Christiansen feature (CF) [Conel, 1969; Logan et al., 1973; Salisbury et al., 1987; Salisbury and Walter, 1989]. The wavelength position of the CF is related to the degree of polymerization of the silicate structure and to a lesser extent, structural changes resulting from cation substitution, resulting in shorter wavelength CF positions for tectosilicates such as feldspar ($\sim 7.33\text{--}7.84$ μm), and longer wavelength CF positions for orthosilicates such as olivine ($\sim 8.5\text{--}9.0$ μm), with pyroxene having intermediate values ($\sim 8.2\text{--}8.3$ μm) [e.g., Nash et al., 1993]. As can be inferred from the

numbers above, CF position alone is not enough to distinguish a plagioclase-olivine mixture from pyroxene. The nonuniqueness of the CF position is why the VNIR is most suited to the identification of olivine-rich, pyroxene-poor regions, while the MIR is useful for placing constraints on abundance. Therefore, we use the unique capabilities of the Diviner instrument along with simulated lunar environment laboratory effective emissivity spectra of plagioclase-olivine mixtures to place effective upper limits on olivine abundance.

As with the VNIR, there are challenges when applying MIR laboratory emissivity data to remote sensing data, particularly for airless bodies. The thermal environment created by vacuum conditions results in substantial changes in the characteristics of emissivity spectra when compared with ambient or even Martian (~ 6 mbar) surface pressures [e.g., Logan *et al.*, 1973; Salisbury and Walter, 1989]. These changes include an overall increase in spectral contrast with decreasing pressure and deepened absorption in the reststrahlen band region, which results in a CF shift to shorter wavelengths [e.g., Logan *et al.*, 1973; Nash *et al.*, 1993]. Within finely particulate materials under a substantial atmosphere, gas conduction is the dominant form of heat transfer. This is not the case for finely particulate materials under very low pressure conditions ($\sim 10^{-3}$ mbar), where the observed increase in spectral contrast is due to steep thermal gradients (a change of tens of kelvins versus a few kelvins within the top 1 mm) produced by radiative cooling at the surface, a process that is much less effective in the presence of gas, which can transfer heat [Logan *et al.*, 1973; Henderson and Jakosky, 1994]. To characterize these effects, several researchers have recently measured simulated lunar environment (SLE) effective emissivity spectra for mineral end-members [Greenhagen *et al.*, 2010; Donaldson Hanna *et al.*, 2012a; Shirley and Glotch, 2015] and assessed the changes in CF position within the plagioclase solid solution series [Donaldson Hanna *et al.*, 2012b]. In this work we measure the behavior of changes in CF for mineral mixtures of plagioclase-olivine and plagioclase-augite. Typically, spectral features of mixtures are assumed to add linearly across the MIR according to their volume abundance [e.g., Adams *et al.*, 1986; Thomson and Salisbury, 1993]. However, this has only been shown to be applicable to larger grain sizes ($>60 \mu\text{m}$) [Ramsey and Christensen, 1998]. Pan and Rogers [2014] demonstrated that mixing behavior of small ($<10 \mu\text{m}$) grains can be nonlinear, especially in spectral regions where the absorption coefficient is low, such as the CF and shortward.

For the reasons outlined above, to support our remote sensing data analysis, we acquired a set of lunar-like environment MIR emissivity spectra of plagioclase-olivine mixtures, for comparison with Diviner remote sensing data, using the instrumentation described in Thomas *et al.* [2012] at the Atmospheric, Oceanic and Planetary Physics Department at the University of Oxford. These data also allow for comparison of the measured mixture spectra to the assumption of linear mixing as well as characterization of the response of Diviner-derived effective emissivity to mixture composition. Assuming, based on SP and M^3 results, that the areas of interest can be modeled as a two-component mixture of olivine and plagioclase, we give upper bounds on the abundance of olivine present at these sites. To account for the effects of space weathering on mineralogical interpretation of Diviner data, we use an albedo-based correction [Lucey *et al.*, 2000, 2010] that shifts the derived CF appropriately as a function of maturity. In addition to the plagioclase-olivine mixtures, we took measurements of plagioclase-augite mixtures to help define an olivine index that can be applied to Diviner data to help identify olivine-enriched areas. Such an index is useful because these areas do not necessarily stand out in a CF map.

2. Data, Methods, and Samples

2.1. Remote Sensing Instruments and Data Processing

2.1.1. Diviner Instrument and Data

Diviner has three narrow-band channels near $8 \mu\text{m}$ centered at $7.80 \mu\text{m}$ (Ch 3), $8.25 \mu\text{m}$ (Ch 4), and $8.55 \mu\text{m}$ (Ch 5), chosen to help pinpoint the position of the Christiansen feature (CF). The CF is an emissivity maximum characteristic of silicates in the range of $7\text{--}9 \mu\text{m}$ followed by a set of absorption bands near $10 \mu\text{m}$, which can be used to characterize the silicate mineralogy of the lunar surface [e.g., Lyon, 1964; Logan *et al.*, 1973; Greenhagen *et al.*, 2010; Paige *et al.*, 2010]. We binned the Diviner data at either 128 or 256 pixels per degree for regional analysis. We selected orbits during which Diviner's spatial resolution is ~ 250 m per pixel. In this work, we also use one of Diviner's thermal channels (Ch 6) covering $13\text{--}23 \mu\text{m}$ to define a spectral index that can be used to identify areas of olivine enrichment. Data were constrained to be less than 50° from the equator and between 10:00 and 14:00 local time. We estimated the maximum brightness temperature of each pixel by fitting the brightness temperatures of Channels 3 through 5 to a parabola. The effective emissivity values

for each channel were then calculated by dividing the measured radiance by the radiance calculated from the estimated maximum brightness temperature. We use the term “effective emissivity” due to the fact that the steep thermal gradients encountered in the lunar environment mean that the estimated brightness temperature differs substantially from the actual range of temperatures contributing to the observed radiance.

The CF of the lunar surface has been observed to change with latitude and local time of day on the lunar surface. To account for this, we apply an empirical photometric correction that compensates for these changes by normalizing the calculated emissivity values to match equatorial noontime conditions [Greenhagen *et al.*, 2011]. Space weathering processes also have a substantial impact on CF position. Compared to unweathered surfaces, the CF positions of mature surfaces are shifted to longer wavelengths with increasing optical maturity [Lucey *et al.*, 2010; Glotch *et al.*, 2015; Lucey *et al.*, 2016].

Compositional information can still be obtained from areas affected by space weathering through the application of an estimate of optical maturity derived from near-IR data. We applied an optical maturity correction derived from Kaguya (SELENE) Multiband Imager (MI) 750 nm and 950 nm albedo data [Lucey *et al.*, 2010] to the Diviner CF. This is an updated version of the Clementine optical maturity (OMAT) index, which is based on a linear relationship between the 950 nm/750 nm ratio and the 750 nm reflectance for lunar soil samples. More mature lunar soils trend toward the redder (higher 950 nm/750 nm ratio) and darker (lower 750 nm reflectance) end of this linear relationship [Lucey *et al.*, 2000]. The empirical correction to the CF based on the OMAT index is $CF_{\text{corr}} = CF + \text{OMAT} - 0.4$. This correction is tied to the spectrally pure anorthite exposure at the central peak of Jackson crater [Ohtake *et al.*, 2009] and brings the Diviner CF values of this location in line with measured laboratory values of nonspace weathered pure minerals. For the areas of interest, this correction shifts the CF by an average of $\sim 0.2 \mu\text{m}$.

The CF also changes with physical properties such as particle size, and to a lesser extent, packing [Logan *et al.*, 1973]. However, the spectrum of the lunar surface is dominated by the smaller size fractions ($< 45 \mu\text{m}$) [e.g., Starukhina *et al.*, 1994; Noble *et al.*, 2000], so that the shift of the CF position with particle size will be much smaller than the shifts due to composition [Aronson and Emslie, 1973; Salisbury and Wald, 1992; Ruff *et al.*, 1997; Ruff and Christensen, 2002]. Differences in packing cause significant changes to the spectral contrast of the reststrahlen bands but have a small impact on the CF position [Logan *et al.*, 1973; Salisbury and Wald, 1992; Donaldson Hanna *et al.*, 2014a].

2.1.2. Moon Mineralogy Mapper (M^3) Instrument and Data

We used VNIR (430–3000 nm) Level 2 reflectance data from M^3 to confirm the location of olivine-bearing regions detected by SP [Yamamoto *et al.*, 2010]. It is important to confirm the exact locations as olivine-rich regions will not stand out on a CF map for concentrations less than 90 vol%, the concentration required to have a longer wavelength CF position than pyroxene. M^3 hyperspectral image cubes have high spatial (ranging from 14070 m per pixel depending on orbit altitude and whether data was collected in “global” or “targeted” mode) and spectral (20 nm sampling, global mode and 10 nm sampling, targeted mode) resolution [Goswami and Annadurai, 2008; Pieters *et al.*, 2009; Boardman *et al.*, 2011]. For comparison, SP data have a spatial resolution of 500 m per pixel and cover the 500–2600 nm wavelength range with a spectral resolution of 6–8 nm [Kato *et al.*, 2008]. The M^3 data set was chosen for three reasons: (1) availability of the data set at the time this work was started [Lundeen, 2011], (2) because M^3 is an imager rather than a profiler, the data set allows direct regional comparison to Diviner effective emissivity data, and (3) M^3 has a comparable spectral range to SP. Reflectance data were obtained from the Planetary Data System (PDS) [Lundeen, 2011]. Due to the significant variations in observation conditions over the lifetime of the mission [Boardman *et al.*, 2011], Table 1a gives the image number, optical period, and number of pixels averaged for each M^3 data strip that was used.

2.2. Simulated Lunar Environment Laboratory Data, Methods, and Samples

To use the Diviner CF to infer lunar surface composition, there are few additional factors that need to be taken into consideration. The thermal emission of the lunar surface is affected by the space environment. We address this by comparing the Diviner data (Table 1b) to spectra acquired in analogous laboratory conditions.

The olivine sample used in this study consists of millimeter-sized forsterite grains from San Carlos, AZ, obtained from Ward's Science and was determined by electron microprobe analysis (Table 2) to be Fo₉₁. The CF position of olivine varies greatly with Fo#. Hamilton [2010] measured MIR emissivity spectra of a

Table 1a. Information for NIR Data of Areas Examined in This Study Including Location, M³ Image Number, Optical Period (OP), Integrated Band Depths (IBD), and Band Positions

Location	M3 Image Number	OP	Description/Notes	Latitude	Longitude	Npts Averaged	1 μ m IBD	2 μ m IBD	1 μ m Band Minimum Position (nm)	2 μ m Band Minimum Position (nm)
<i>A: Mare Moscoviense</i>										
A2	M3G20090528T130108	2C	S crater ejecta	28.1	145.3	18	0.5638	0.1328	1063	2297
A3	M3G20090528T083319	2C	S wall of small crater	21.35	147.16	24	0.3691	0.0041	1045	--
A3	M3G20090528T083319	2C	NE wall of small crater	21.07	147.36	24	0.8508	0.1176	1050	2314
A4	M3G20081229T022350	1A	W crater wall and ejecta	22.86	148.94	154	0.5274	0.4294	1058	2138
A5	M3G20090528T130108	2C	SW crater wall	21.85	146.47	45	0.3795	-0.0123	1061	--
A6	M3G20081229T022350	1A	S crater wall	21.64	148.15	47	0.4809	0.123	1050	2063
A7	M3G20081229T180950	1A	W crater wall	23.01	139.77	187	0.1765	0.0236	1098	--
<i>B: Mare Crisium</i>										
B1	M3G20090105T134845	1A	Glaisher crater wall	13.24	49.14	283	0.8742	0.101	1048	2326
B1	M3G20090105T134845	1A	WSW wall Glaisher crater	13.23	49.19	9	0.7831	0.431	1085	2228
B1	M3G20090105T134845	1A	N of Glaisher crater	13.66	49.19	9	0.1587	-0.0913	1045	--
B1	M3G20090105T134845	1A	SE wall Glaisher crater	13.01	49.52	9	0.8055	0.0987	1005	1976
B2	M3G20090131T151551	1B	SW crater ejecta	12.03	65.55	47	0.6736	0.0418	1045	--
B3	M3G20090104T062425	1A	Pr. Agarum	14.25	66.15	88	0.1399	0.3411	1043	2093
B4	M3T20090104T220845	1A	NE crater ejecta	8.42	58.69	40	0.6364	0.0421	1053	--
B4	M3T20090701T140225	2C	nearby NW crater ejecta	8.85	59.13	82	0.331	0.1078	1052	2208
B6	M3G20090201T165935	1B	SW crater wall (noisy in M3)	11.95	52.41	154	0.485	0.2936	1064	2206
<i>C: Mare Imbrium</i>										
C1	M3G20090416T122951	2A	Copernicus central peak	9.63	339.96	29	1.2473	-0.1215	1064	--
C1	M3G20090416T122951	2A	N wall Copernicus	10.96	339.97	9	4.4514	-0.7401	1153	--
C1	M3G20090416T122951	2A	central peak Copernicus main	9.68	339.93	9	1.8712	-0.3797	1099	--
C1	M3G20090416T122951	2A	central peak Copernicus small	9.65	340	9	1.2048	0.8039	1068	2154
C2	M3G20090608T125102	2C	S-facing M3 olv spot	44.85	359.18	9	0.705	3.1352	1059	2148
C3	M3G20090609T101951	2C	Eratosthenes crater central peak	14.63	348.88	18	0.7694	0.7772	1039	2165
C4/5	M3G20090208T021836	1B	crater wall?	48.2	329.2	30	1.3621	0.0707	1016	--
C6	M3G20090612T060502	2C	Aristarchus crater rim	23.35	313.02	284	2.2078	0.6836	1040	2157
<i>D: Mare Humorum</i>										
D1	M3G20090612T060502	2C	W crater wall	-19.25	312.73	136	0.3889	0.3419	1047	2159
D1	M3G20090209T054031	1B	W crater wall	-19.3	312.78	9	1.6167	0.8022	1152	2131
<i>G: Mare Nectaris</i>										
G1	M3G20090107T011405	1A	crater wall in mare	-14.45	30.07	96	2.4061	0.6836	1054	2191
G2	M3G20090203T160452	1B	central peak theophilus	-11.25	26.38	379	0.5616	-0.0194	1044	--
<i>H: Mare Serenitatis</i>										
H1	M3G20090108T044645	1A	crater wall E	16.29	16.22	9	0.4424	0.4445	1105	2136
<i>J: Mare Australe</i>										
J1	M3G20090601T062753	2C	small crater S wall	-33.47	97.12	76	0.8254	0.402	1050	2085
<i>Mare Nectaris</i>										
Pyroxene	M3G20090107T011405	1A	W crater wall	12.57	30.98		2.3989	2.0793	991	2155

Table 1b. Information for MIR Data of Areas Examined in This Study Including Location, CF and OMAT Values, and Olivine Abundance Estimates^a

Location	Description/Notes	Standard CF			Corrected CF			Npts Averaged	MI-OMAT	Clementine-OMAT	CF + OMAT -0.4	Olivine Based On Two-Component System (%)	Olivine Range Based On CF Uncertainty (%)
		Position	σ	CF	Position	σ	CF						
<i>A: Mare Moscoviense</i>													
A2	S crater ejecta	28.10	145.30	8.51	0.12	0.06	256	42	0.1719	--	8.1869	71	61-84
A3	S wall small crater	21.35	147.16	8.60	0.07	8.32	0.02	128	10	0.1702	8.0894	58	49-63
A3	NE wall small crater	21.07	147.36	8.32	0.01	8.42	0.05	128	10	0.1845	8.2016	73	64-85
A4	W crater wall ejecta	22.86	148.94	8.50	0.12	8.34	0.03	256	42	0.1182	8.0582	52	41-59
A5	SW crater wall	21.85	146.47	8.51	0.14	8.42	0.10	256	23	0.1389	8.1589	67	50-85
A6	S crater wall	21.64	148.15	8.14	0.08	8.27	0.03	256	22	0.1471	8.0171	42	28-52
A7	W crater wall	23.01	139.77	8.21	0.04	8.15	0.02	256	270	0.1609	7.9109	12	6-22
<i>B: Mare Crisium</i>													
B1	Glaisher crater wall	13.24	49.14	8.24	0.06	8.22	0.06	256	440	0.1741	7.9941	35	12-52
B1	WSW wall Glaisher crater	13.23	49.19	8.36	0.01	8.29	0.04	128	12	--	8.1042	60	50-67
B1	N of Glaisher crater	13.66	49.19	8.33	0.02	8.14	0.02	128	8	0.2093	7.9482	20	10-34
B1	SE wall Glaisher crater	13.01	49.52	8.24	0.02	8.13	0.03	128	12	0.2080	7.9450	19	9-35
B2	SW crater ejecta	12.03	65.55	8.41	0.02	8.27	0.02	256	51	0.2190	8.0093	40	27-50
B3	Pr. Agarum	14.25	66.15	8.40	0.10	8.35	0.07	256	105	0.1374	8.0874	57	40-68
B4	NE crater ejecta?	8.42	58.69	8.43	0.03	8.33	0.04	256	55	0.1405	8.0705	55	42-62
B4	nearby NW crater ejecta	8.85	59.13	8.50	0.06	8.37	0.03	256	196	0.1195	8.0895	58	48-63
B6	SW crater wall (noisy in M3)	11.95	52.41	8.94	0.58	8.43	0.40	256	215	0.1447	8.1747	69	1-94
<i>C: Mare Imbrium</i>													
C1	Copernicus central peak	9.63	339.96	8.35	0.20	8.23	0.18	256	41	0.2235	8.0535	51	6-81
C1	N wall Copernicus	10.96	339.97	8.37	0.03	8.25	0.02	128	12	--	8.0865	57	49-62
C1	central peak Copernicus main	9.68	339.93	8.30	0.05	8.10	0.03	128	8	0.2338	7.9762	29	13-44
C1	central peak Copernicus small	9.65	340.00	8.26	0.02	8.14	0.02	128	12	0.2795	7.9878	33	20-45
C2	S-facing M3 olv spot	44.85	359.18	8.20	0.01	8.20	0.02	128	8	0.2434	8.0519	51	41-57
C3	Eratosthenes crater central peak	14.63	348.88	8.56	0.24	8.44	0.10	256	42	0.2568	8.2113	75	59-90
C4/5	crater wall?	48.20	329.20	8.26	0.21	8.22	0.02	256	42	--	7.9661	26	12-40
C6	Aristarchus crater rim	23.35	313.02	8.27	0.14	8.24	0.05	256	313	0.2967	8.1367	64	54-73
<i>D: Mare Humorum</i>													
D1	W crater wall	-19.25	312.73	8.33	0.05	8.27	0.03	256	340	0.1722	8.0422	49	36-56
D1	W crater wall	-19.30	312.78	8.34	0.03	8.34	0.03	128	15	0.2250	8.1649	68	61-76
<i>G: Mare Nectaris</i>													
G1	crater wall in mare	-14.45	30.07	8.58	0.20	8.48	0.10	256	171	0.2073	8.2873	87	70-97
G2	central peak theophilus	-11.25	26.38	8.17	0.09	8.12	0.04	256	592	0.2309	7.9509	21	9-39
<i>H: Mare Serenitatis</i>													
H1	crater wall E	16.29	16.22	8.19	0.01	8.18	0.01	128	20	0.2131	7.9903	34	22-45
<i>J: Mare Australe</i>													
J1	small crater S wall/floor	-33.33	97.15	8.29	0.02	8.23	0.02	128	12	0.2284	8.0591	52	43-58

^aStandard CF values are before latitude/time of day correction.

Table 2. Electron Microprobe Data for Anorthite, Forsterite, and Augite Samples Included in Lunar Environment Emissivity Measurements^a

Source	<i>anorthite</i>	<i>forsterite</i>	<i>augite</i>
	SBU	Wards	SBU
Na ₂ O	0.404	0.003	0.495
2σ	0.239	0.005	0.041
K ₂ O	0.002	--	--
2σ	0.209	--	--
MgO	0.094	49.753	11.85
2σ	0.098	0.597	0.166
Al ₂ O ₃	35.016	0.022	0.513
2σ	1.129	0.012	0.03
FeO	0.459	8.92	10.057
2σ	0.231	0.281	0.302
SiO ₂	42.624	40.675	51.956
2σ	1.139	0.326	0.416
CaO	19.747	0.088	23.742
2σ	1.722	0.016	0.344
TiO ₂	0.003	0	0.019
2σ	0.099	0	0.018
MnO	0.004	0.123	0.27
2σ	0.153	0.034	0.048
Cr ₂ O ₃	-0.001	0.011	0.023
2σ	0.016	0.01	0.029
Total	98.37	99.595	98.925
	An# = 96 (+3.3/−3.7)	Fo# = 90.9 (+0.3/−0.4)	Fo# = 67.7 (+1.0/−0.9)

^aMicroprobe data for anorthite were collected at the Natural History Museum in London. Microprobe data for forsterite and augite were collected at Stony Brook University. Errors listed on An and Fo numbers take 2σ errors on oxide wt % into account.

range of olivine samples from Fo₉₂ to Fo₀ under normal atmospheric pressure, which had CF positions of 8.62 to 9.33 μm, respectively. However, an observed CF on the lower end of this range could be due to either olivine with a high Fo# or an olivine with lower Fo# mixed with any mineral of a lower CF value such as, in the case of our regions of interest, plagioclase. Since our goal is to establish upper limits for olivine concentration, we chose a composition toward the forsteritic end of lunar olivine as listed in reviews compiling a large number of studies: Mg-troctolite (Fo_{73–90}) and dunite (Fo_{87–89}) [Heiken *et al.*, 1991; Wieczorek *et al.*, 2006]. Moreover, this is similar to the composition that Yamamoto *et al.* [2010] found produced the best fits to SP data of olivine-rich regions (Fo₉₀). Augite (En₂₆Wo₅₂Fs₂₃) was obtained from Ward's, and its composition was measured with both electron microprobe (Table 2) and powder X-ray diffraction. The plagioclase sample consists of ~1 cm anorthite single crystals originating from Miyake Jima, Japan. This particular composition was selected for its similarity in An# (100 × Ca/[Ca + Na + K]) to plagioclase in both ferroan anorthosites (An₉₄–An₉₈) and troctolites (An₉₃–An₉₈) [Warren, 1993]. Both the measured lunar environment CF position (7.83 μm) and the estimated "Diviner" CF (defined in the next section) position (7.72 μm) for this sample are comparable to previously measured values for Miyake Jima anorthite [cf. Donaldson Hanna *et al.*, 2014b]. Microprobe analysis (Table 2) gave a high An# value of An₉₆, similar value to that of lunar anorthite and matching that of Donaldson Hanna *et al.* [2014b] who measured a different sample from the same source region. The pure minerals were ground and dry-sieved to <63 μm. Seven samples were prepared ranging from 100 wt % anorthite to 100 wt % forsterite and four samples ranging from 100 wt % anorthite to 100 wt % augite (listed in Table 3).

The samples were placed into a cup with wider surface area than the spectrometer field of view to avoid measuring lateral thermal gradients in the sample. Each time, the sample was placed in the cup, and the excess sample was wiped away with a sharp edge to create a relatively smooth top surface. We acquired laboratory effective emissivity measurements in two configurations for each sample (Figures 2a and 2b). We first acquired ambient spectra in a ~1 bar N₂ atmosphere with the sample cup heated from below to 353 K with no lamp illumination from above. The ambient environment data confirm that any atmospheric contaminants have been removed from the chamber. Additionally, we are also interested in any differences in spectral mixing behavior between ambient and lunar thermal environments, as there has been no experimental data reported on this topic.

Table 3. Mixtures Measured in Lunar Environment Emissivity Chamber^a

Plagioclase wt %		0	12.6	25	50	75	87.4	100
Forsterite	vol %	100	85	71	45	22	11	0
	Measured ambient environment CF	8.61	8.59	8.30	8.26	8.20	8.17	8.11
	Estimated Diviner ambient environment CF	8.92	8.55	8.41	8.31	8.17	8.15	8.13
	Measured lunar environment CF	8.46	8.26	8.21	8.05	7.98	7.87	7.86
	Estimated Diviner lunar environment CF	8.47	8.27	8.19	8.03	7.96	7.92	7.72
	Max Lunar environment T _B (K)	362	380	363	347	353	326	321
	SLE Olivine Index	0.0154	-0.0055	-0.0170	-0.0463	-0.0506	-0.0544	-0.1013
Augite	vol %	100	--	21	44	--	--	0
	Measured ambient environment CF	8.46	--	8.27	8.21	--	--	8.09
	Estimated Diviner ambient environment CF	8.54	--	8.35	8.30	--	--	8.14
	Measured lunar environment CF	8.41	--	8.16	8.09	--	--	7.82
	Estimated Diviner lunar environment CF	8.37	--	8.15	8.03	--	--	7.71
	SLE Olivine Index	0.0034	--	-0.0245	-0.0591	--	--	-0.0875

^aMixtures were made according to weight percentage, equivalent volume percentage of forsterite given in table for reference.

We then acquired simulated lunar environment spectra at a pressure of high vacuum ($<10^{-3}$ mbar, note: "low," "middle," and "high" refer to the degree of vacuum and go in the opposite sense from the pressure) with the chamber cooled to ~153 K, the sample cup heated from below to 393 K, and a 75 W lamp illuminating the sample from above. This configuration causes strong thermal gradients in the optical surface of the sample, producing the spectral contrast enhancements and CF shifts similar to those observed on the Moon [Thomas et al., 2010; Thomas et al., 2012; Donaldson Hanna et al., 2012a]. The lamp output was adjusted with the aim of achieving brightness temperatures of 350–370 K at the CF. However, three samples fell outside this range: the 12.6 wt % anorthite sample which turned out higher (380 K) and the two highest anorthite abundances, which due to their high albedo were difficult to heat to more than 320 K. The sample with

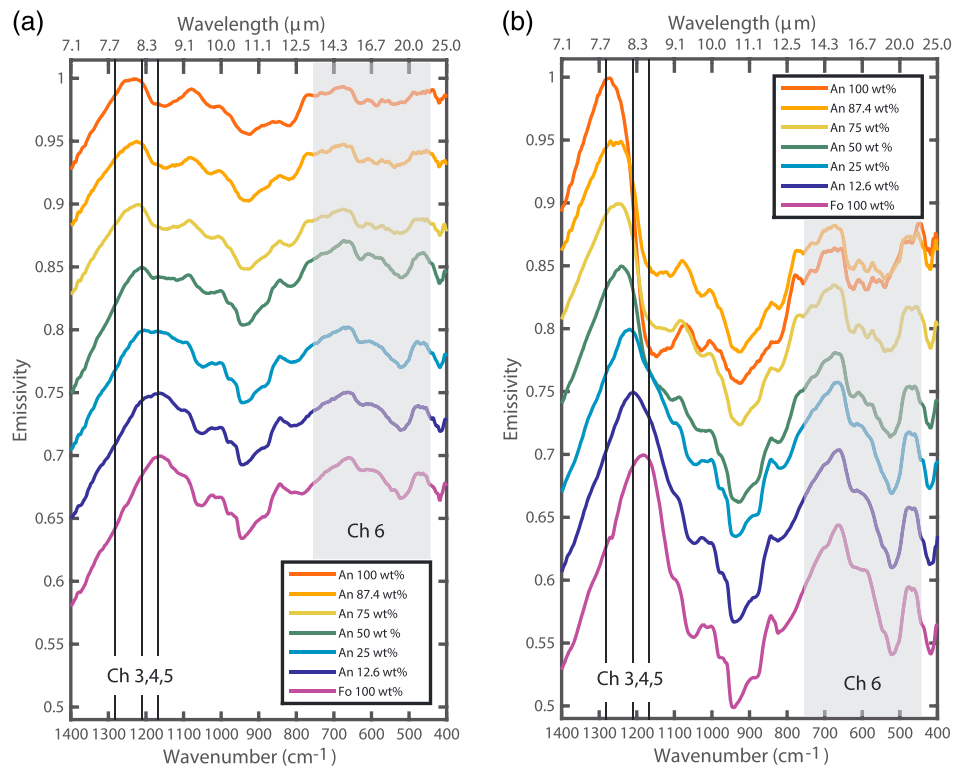


Figure 2. Full-resolution emissivity for plagioclase-olivine mixtures with the approximate locations of Diviner narrow spectral Channels 3–5, near the Christiansen feature, and broadband thermal channel 6. (a) Ambient environment emissivity data. (b) Lunar environment emissivity data. Offset from top of 0.05 for clarity.

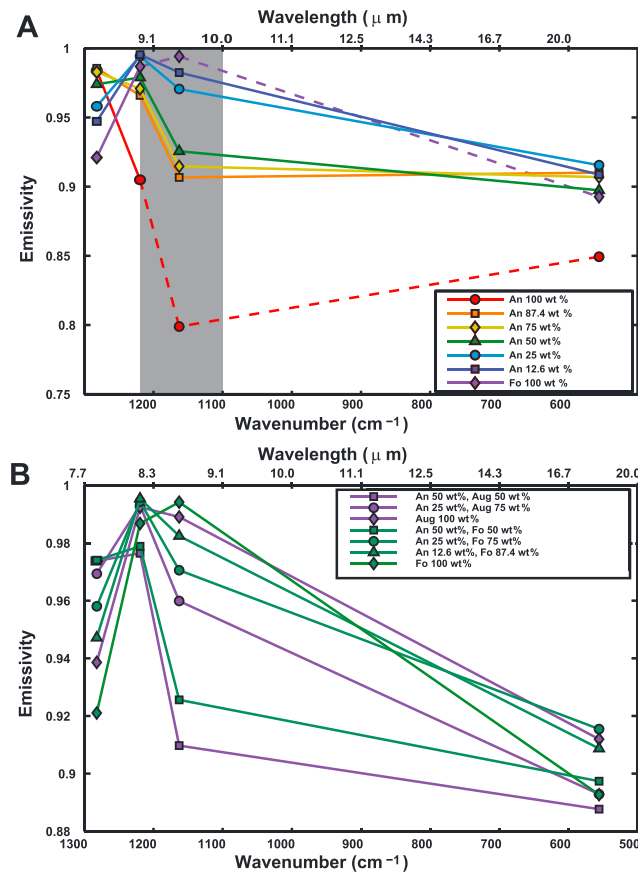


Figure 3. Laboratory emissivity spectra convolved to Diviner spectral resolution and demonstration of the concavity change in Channels 4–6 for both olivine and augite. (a) Lunar environment emissivity spectra of plagioclase-olivine mixtures showing the change in concavity of Ch 456 with mixture composition. The area of concavity change used to derive our olivine index is highlighted in grey. (b) Lunar environment emissivity spectra for selected plagioclase-olivine and plagioclase-augite mixtures convolved to Diviner Channels 4–6.

wavelengths longer than the CF region, extending through one of Diviner’s thermal channels (Channel 6, 13–23 μm). Diviner Ch 6 occurs within a wide region of absorption due to the reststrahlen bands (RB) and transparency features of silicate minerals, and can be used to give some indication of the spectral shape of this region. For a comparison of full resolution simulated lunar environment emissivity spectra with the ranges of Ch 3–5 (narrowband “8 μm” channels) and Ch 6 (a broadband thermal channel) see Figure 2a. To generate our olivine index, we use a concavity index similar to that of *Glotch et al.* [2010, 2011], but including a thermal band (Ch 4, 5, and 6) rather than only using the 8 μm channels (Ch 3, 4, and 5). The full resolution spectra are first resampled to the Diviner channels, and then the index is calculated as follows:

$$\begin{aligned}
 x1 &= 8.28 \text{ (Ch4 center wavelength)} \text{ and } y1 = \text{Ch4 emissivity} \\
 x2 &= 8.55 \text{ (Ch 5 center wavelength)} \text{ and } y2 = \text{Ch5 emissivity} \\
 x3 &= 17.99 \text{ (Ch 6 center wavelength)} \text{ and } y3 = \text{Ch6 emissivity} \\
 \text{Olivine Index} &= y2 - \left(\frac{(y3 - y1)}{(x3 - x1)} \cdot (x2 - x1) \right) + y1
 \end{aligned}$$

Applying this formula to our mixtures, we found that pure anorthite is strongly concave up (negative index value), pure augite is weakly concave down (small positive index value), and olivine is strongly concave down (larger positive index value). Figure 3 illustrates this change in concavity for our laboratory spectra convolved to Diviner channels of olivine-anorthite (Figure 3a) and augite-anorthite (Figure 3b) mixtures and index values for these same mixtures are given in Table 3. Because an incidence angle correction for Ch 6 is still under development [*Shirley and Glotch, 2014*], we cannot presently include this correction

12.6 wt% anorthite has a CF position in-between those of the 0wt% and 25 wt% samples, despite having been heated to a higher temperature than those two samples. Moreover, the 0wt% and 25 wt% anorthite samples were measured at nearly the same brightness temperatures and have a large difference in CF, indicating that composition is a much more important effect. The maximum brightness temperatures of all olivine-anorthite mixture samples are given in Table 3. Although there appears to be some relationship between CF and brightness temperature (see Figure S4 in the supporting information), this is mostly due to sample transparency and visible albedo having an effect on the brightness temperature we can achieve. While albedo influences the thermal gradient in the sample, and therefore the CF, albedo itself is linked to the sample’s composition. Additional details regarding sample preparation, data acquisition, and calibration are described in *Thomas et al.* [2012].

2.3. Remote Sensing Data Analysis Methods

2.3.1. Olivine Spectral Index From Diviner Data

We used the MIR spectra obtained under conditions simulating the lunar radiative environment to develop a spectral index for olivine. The simulated lunar environment emissivity data include

Table 4. Areas Excluded From This Survey

Location	Latitude	Longitude	Reason Excluded
A1	32.5	<i>A: Mare Moscoviense</i> 143.5	No Diviner coverage at time of study
B5	24.11	<i>B: Mare Crisium</i> 54.20	Could not locate olivine with M ³ Olivine spot too small (<9 pix)
B7	18.81	49.63	
E1	−72.1	<i>E: Schrödinger Crater</i> 133.8	Latitude too high
E2	−76.3	143.1	Latitude too high
E3	−76.2	130.6	Latitude too high
F1	53.35	<i>F: Frigoris</i> 103.50	Could not locate olivine with M ³
I1	53	<i>I: Mare Humboldtianum</i> 102.3	Could not locate olivine with M ³
J2	−27.09	<i>J: Mare Australe</i> 83.13	Olivine spot too small (<9 pix)
K1	33.99	<i>K: W. Side of Oceanus Procellarum</i> 300.82	Olivine spot too small (<9 pix)
L1	35.40	<i>L: Geminus</i> 56.57	Olivine spot too small (<9 pix)
M1	−74.9	<i>M: Zeeman</i> 225.9	Latitude too high

in the olivine index. However, we note that when this correction is applied at low resolution, it tends to push this index toward less mafic values (smaller values). While this index cannot be used to directly calculate abundance, this index can be used to gauge the relative abundance of olivine in a scene, which is helpful for identifying the olivine enriched regions in Diviner data, as they do not always stand out in a CF map.

2.3.2. M³ and Diviner Data Analysis for Regional Comparisons

For each area of interest, we generated index maps of the 1 μm and 2 μm integrated band depths (IBD) from M³ reflectance data. Band depths are calculated by summing the difference between the actual reflectance and the continuum as fit by a line over the absorption bands (790 nm to 1309 nm for the 1 μm IBD and 1659 to 2497 nm for the 2 μm IBD; note within the M³ data bands are given in nanometer) [Mustard *et al.*, 2011]. Values for 1 μm IBD and 2 μm IBD as well as band minimum positions are given in Table 1a. Band positions were determined using Gaussian fits. In this table, we also present these values for a typical lunar pyroxene spectrum (location given in Table 1a), with a strong 2 μm band. We checked the locations of SP olivine detections for a strong 1 μm band, weak 2 μm band, and long wavelength 1 μm band position (between 1 and 1.15 μm). Of the 33 SP regions of interest, we were able to confirm 25 detections. Three of the locations identified by SP did not show any nearby areas with characteristic olivine absorptions in M³ data, and positive detections in these locations may be due to an unusually strong 1.25 μm Fe²⁺ band of plagioclase we identified in these regions. Four of the locations are at high latitude where M³ signal-to-noise is low and the corrections to Diviner radiance values for latitude and time of day are limited, affecting the estimated CF position. One of the areas did not have adequate Diviner coverage. Of the 25 confirmed M³ detections, 4 of the locations, while visible with M³, were not spatially extensive enough to be seen with Diviner's spatial resolution. Our cutoff was less than 3 \times 3 M³ pixels. This leaves a total of 21 locations for combined M³ and Diviner data analysis (Table 4 details all areas excluded from this study). For these confirmed detections, we extracted M³ spectra from these regions and applied a convex hull continuum removal (see Isaacson *et al.* [2011] for a discussion of continuum removal techniques for M³ spectra of olivine-enriched areas). The continuum tie points were 700 nm and 2576 nm. The long wavelength cutoff was chosen in order to avoid most of the region that includes a contribution from thermal emission which causes an additional slope change in the continuum that can affect the location and width of the 2 μm pyroxene band where present [Klima *et al.*, 2011]. The locations of the 1 μm and

2 μm band minima were estimated by a Gaussian fit to the continuum removed 1 μm and 2 μm regions (Table 1a). We used the accompanying M^3 location files to extract the coordinates of spots with a high 1 μm IBD index value, but lower 2 μm IBD index and a large enough spatial extent to be visible at Diviner's spatial resolution.

Using M^3 locations of these spots as a guide, we then extracted MIR effective emissivity derived from Diviner radiance measurements for all locations where data were available (Table 1b). To minimize the effects of surface anisothermality [Greenhagen *et al.*, 2010; Bandfield *et al.*, 2015], we only used daytime data constrained to less than 50° latitude from the equator and applied the solar incidence angle correction described in section 2.1.1. Even with the latitude and daytime spatial coverage restrictions, Diviner data are available for 21 confirmed SP regions of interest. Some locations had a few areas of interest within the M^3 data near the SP spots, and including these, we collected CF data for 30 total spots. Each additional area of interest was within the same feature as, but not contiguous to, the reported SP spot location. Diviner effective emissivity and M^3 reflectance spectra were extracted from and averaged over polygons covering nearly identical spots on the lunar surface (Figure 4). There were small spatial offsets due to the different geodetic standards and uncertainties related to the Chandrayaan-1 and Lunar Reconnaissance Orbiter (LRO) mission data. We used images from the Lunar Reconnaissance Orbiter Camera (LROC) wide-angle camera (WAC), which is used to topographically project Diviner data, to verify the locations and make small adjustments (typically a few pixels) to the areas of data extraction when necessary.

3. Results

3.1. Lunar Environment and Ambient Laboratory Data

Full-resolution spectra obtained under simulated lunar conditions of the end-members and mixture samples are shown in Figure 2. For direct comparison between laboratory and Diviner remote sensing data, we convolved the full-resolution spectra to Diviner's filter functions for Channels 3–6 (7.80 μm –23 μm). Convolved spectra are shown in Figure 3. We calculated the CF wavelength position of each mixture based on the convolved emissivities (listed in Table 3) in the same manner as the Diviner data [Greenhagen *et al.*, 2010]. We also calculated CF positions based on a linear mixture of our end-member spectra using both the full-resolution and Diviner-convolved generated spectra (Table 3 and Figure 7). The nonlinearity of mixing is more apparent at longer wavelengths corresponding to Channels 5 and 6 (see Figures 3a and 3b). In both ambient and simulated lunar conditions, the spectra and calculated CF's deviate from a linear mixing trend; however, the shapes of the CF curves are different in each case, with the measured ambient values farther from the linear mixing trend for lower wt% values of anorthite and the measured simulated lunar values farther from the linear mixing trend at higher wt% values of anorthite. Though the calculated CF's of the lunar environment mixture spectra are close to the linear mixing trend derived from the end-members for lower weight percentages of anorthite, there is a substantial departure (about 0.1 μm) for greater than 50 wt% anorthite. The nonlinear response of the CF is stronger toward the end-member compositions in both cases.

3.2. Diviner Olivine Index

We applied our olivine index, based on concavity changes seen in laboratory data, to Diviner effective emissivity data and compared the resulting maps with Diviner CF maps. Figure 5 shows side-by-side maps of our olivine index and CF position for the southeast rim of Aristarchus as well as Promontorium Agarum in the SE rim of Mare Crisium. Our olivine index, compared to a CF map, more strongly highlights the olivine-enrichment in the southwest rim of Aristarchus as well as an area of ejecta to the south. This provides us with a check on the boundaries of the olivine-enriched areas, in addition to the coordinates from M^3 and the LROC WAC base map, as these areas do not necessarily stand out in a Diviner CF map. Figure 6 is a plot of our olivine index versus CF for the same two regions. While the two values are correlated there is a turnoff in index values toward very long wavelength CF positions. This turnoff is likely caused by the nonlinear relationship between Diviner CF values and full resolution CF positions at long wavelengths (SOM) [Greenhagen *et al.*, 2010]. Moreover, for a given CF value, there is a spread in index values, indicating that the index provides compositional information unavailable by assessing CF position alone.

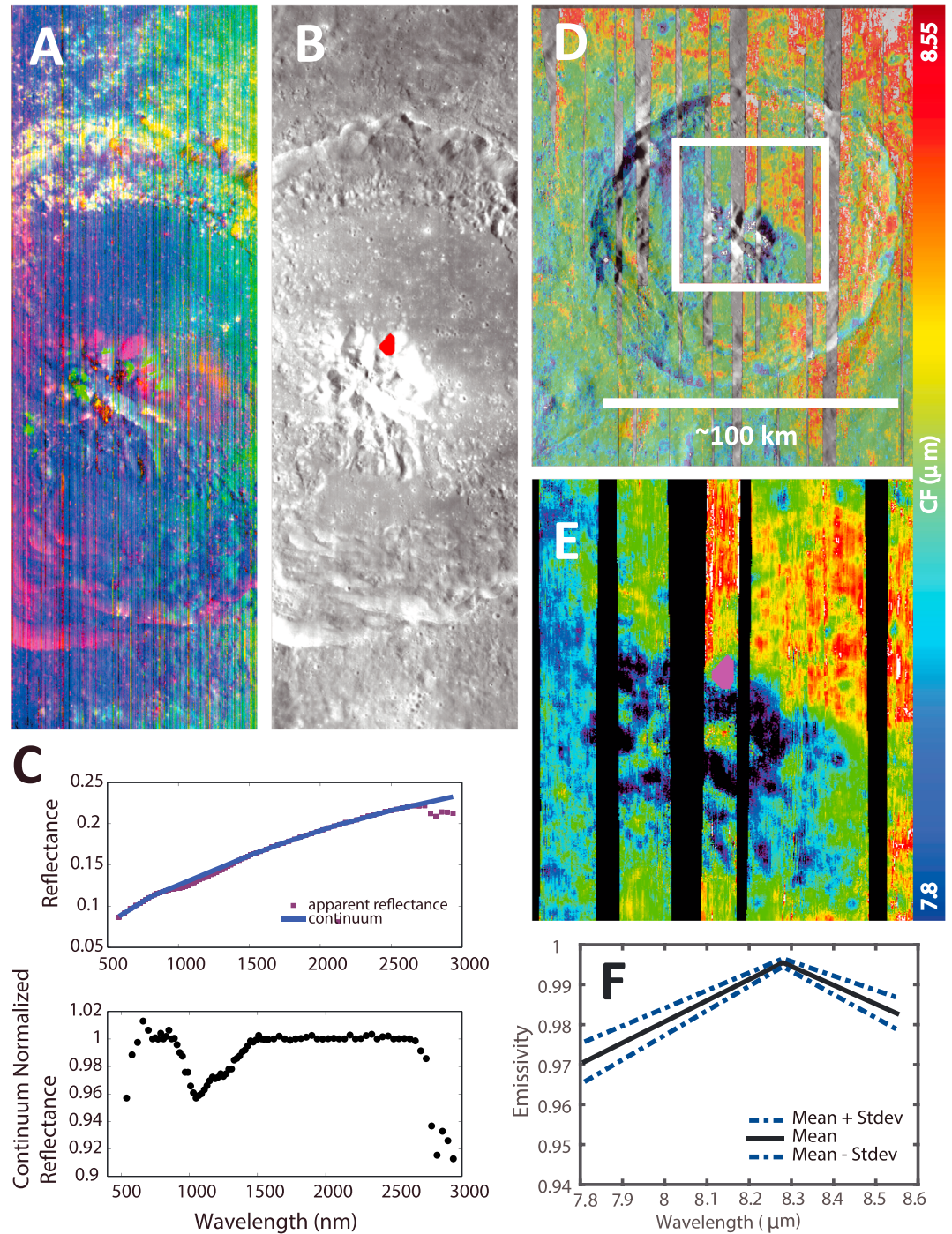


Figure 4. Example area of interest, Theophilus Crater, where red and magenta polygons indicate the areas of data extraction. (a) M^3 index map where red = 1 μm band depth, green = 2 μm band depth and blue = 1.578 μm reflectance along with (b) 700 nm reflectance. (c) M^3 raw reflectance spectrum and continuum removed reflectance spectrum. (d) Diviner CF map stretched 7.8 μm to 8.55 μm . Base map is LROC WAC. (e) Diviner CF map of area in white box above stretched 7.8 μm to 8.55 μm . (f) Diviner emissivity data.

3.3. Plagioclase-Olivine Ratios from Diviner CF

Most olivine-enriched areas that we have investigated have a weak or absent 2 μm band in the VNIR spectra, indicating that these regions have low pyroxene abundances, allowing us to model Diviner data as a two-component olivine-plagioclase system based on the laboratory mixture spectra.

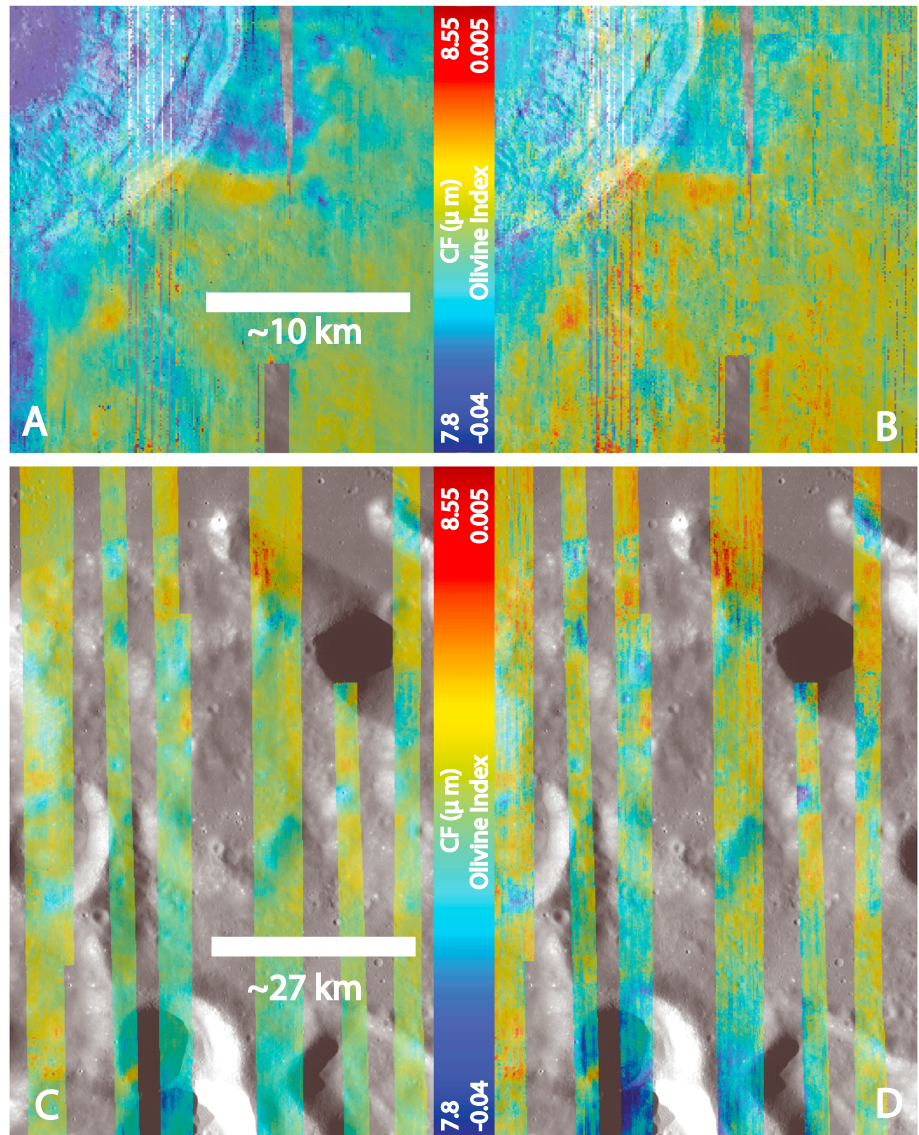


Figure 5. Comparison of CF with Ch 456 concavity at (a and b) Aristarchus crater and (c and d) Pr. Agarum. (a and c) Diviner CF maps scaled 7.8 μm (blue) to 8.55 μm (red). (b and d) Ch 456 olivine index scaled -0.04 (blue) to 0.005 (red). Base maps are LROC WAC.

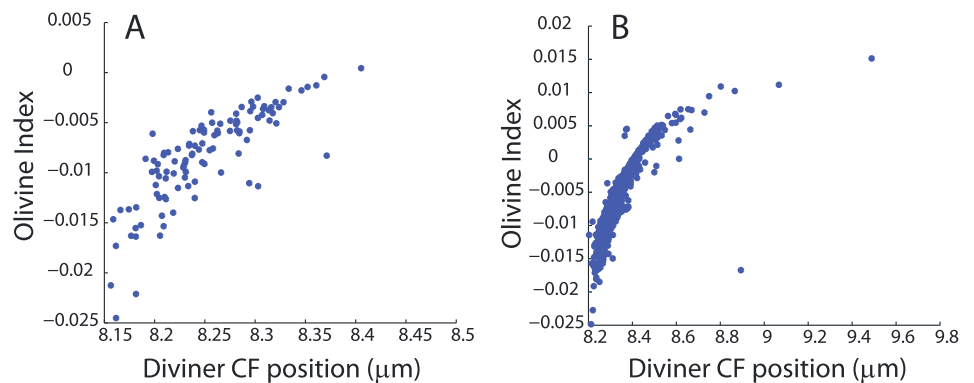


Figure 6. Plot of Ch 456 olivine index versus Diviner CF for the southwest rim of (a) Aristarchus crater and (b) Pr. Agarum. The CF values have been corrected for incidence angle effects, but not for soil maturity/space weathering.

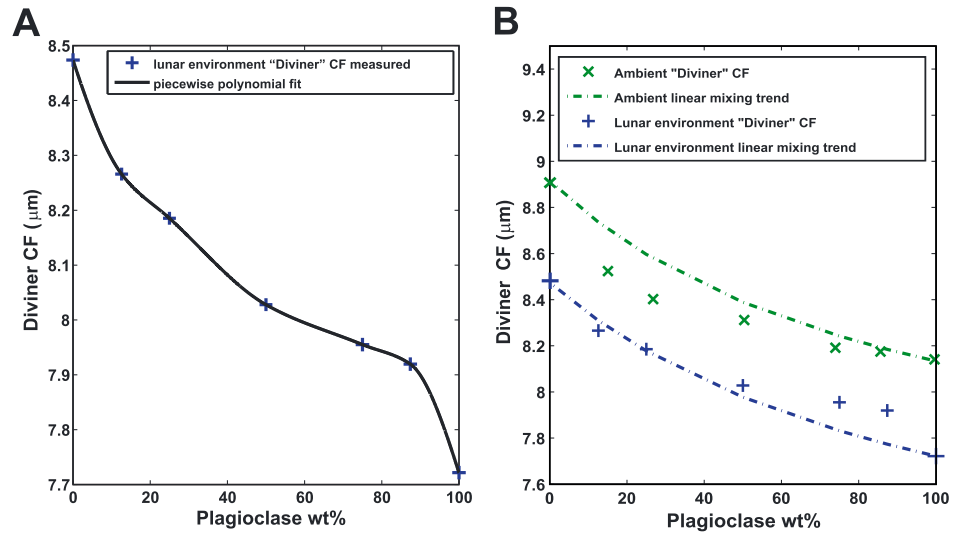


Figure 7. (a) Calculated Diviner CF values lunar environment data with piecewise polynomial fit used to provide a calibration curve for Diviner remote sensing data. (b) Calculated Diviner CF values from both ambient and simulated lunar environment data, along with the expected trend resulting from linear mixing of the 100% end-member plagioclase and olivine spectra.

From our convolved laboratory data (Figure 3a), we plotted anorthite abundance against lunar environment CF and fit it with a piecewise cubic interpolation function (MATLAB, pchip). We used the resulting abundance versus CF curve (Figure 7) to estimate olivine abundance from the Diviner CF (see histogram in Figure 8b). Based on this calibration, the areas in this study have a wide range of calculated olivine abundances, ranging from ~12% to ~87% (Table 1b). We include uncertainties on the abundance estimates in Table 1b based on (1) a 0.03 error in CF position resulting from uncertainties in the laboratory emissivity measurements [Thomas *et al.*, 2012], (2) a 0.02 error in CF position associated with the latitude/time of day correction [Greenhagen *et al.*, 2010], and (3) the standard deviation of the CF values within the scene.

As discussed in section 2, these numbers represent *upper limits*, as the CF of more fayalitic olivine occurs at longer wavelengths, driving down the necessary abundance of olivine to produce the observed CF position. While the olivine used in laboratory measurements for this study has a composition of Fo₉₁, lunar olivine consists of a wide range of Fo#, e.g., mare basalts (Fo₃₀–80) [Kaula *et al.*, 1981; Papike *et al.*, 1991], alkali-suite

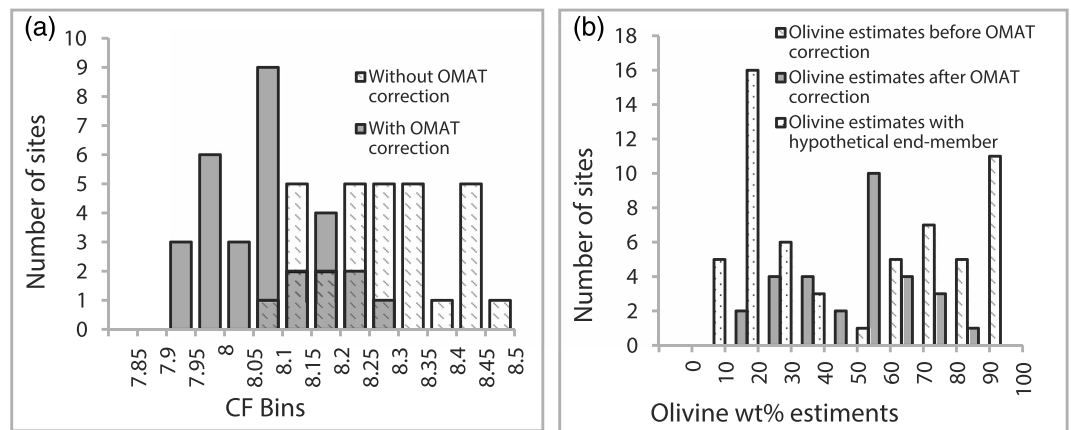


Figure 8. Histograms of (a) CF values of the areas examined in this study both before optical maturity correction (stripes) and after (grey) (b) olivine abundance estimates. Three sets of abundance estimates are given based on CF values prior to optical maturity correction (stripes) CF values after optical maturity correction (grey) and CF values of a hypothetical olivine end-member with a CF of 9 μm (dots), which we estimate would correspond to a Fo₄₀ olivine.

(Fo40–80), Mg-troctolite (Fo73–90), and dunite (Fo87–89) [Heiken *et al.*, 1991; Wieczorek *et al.*, 2006]. Although we do not have lunar environment emissivity measurements over a wide range of Fo#, the CF positions of ambient environment olivine spectra were tabulated by Hamilton [2010]. Olivine compositions in that study included Fo₃₉, close to the lower end for the alkali-suite, and Fo₆₈ close to the lower end of the Mg-suite, which have CF positions of 9.21 μm and 9.02 μm , respectively. Using the linear fit for lunar environment CF versus ambient CF of mineral powders given in Donaldson Hanna *et al.* [2012a], this would lead to estimated SLE CFs of 8.97 μm and 8.77 μm , respectively. These values for fayalitic olivine are longward of Ch 5 (8.3–8.6 μm) but would be distinguishable by a concave up spectral shape in Diviner Ch 3–5, with Ch 5 emissivity greater than Ch 3 [Greenhagen *et al.*, 2010]. Both the longer wavelength CF position of fayalitic olivine and its unique spectral shape would make it readily detectable by Diviner and would also lower the threshold for olivine detectability in mixture. Figure 8b shows how these abundance estimates change if a calibration curve with the same shape as in Figure 7 is applied to a more Fe-rich or fayalitic olivine end-member, with a CF position of 9 μm .

4. Discussion

4.1. Laboratory Lunar Environment Data

Laboratory spectra of plagioclase-olivine mixtures do not always show a single CF but can look like either two peaks or a peak with a shoulder. Therefore, we use estimated Diviner CF positions, calculated by convolving both the laboratory and modeled “linearly mixed” end-member spectra, for comparison with Diviner data. The differences between these projected CF positions and the actual positions of the emissivity maxima of the full resolution spectra are greater for the end-members than the mixtures. The estimated Diviner CF positions of our anorthite-forsterite mixtures do not follow the trend for linearly mixed spectra with composition in either an ambient or lunar environment (Figure 7). Moreover, departure from a linear trend occurs at different olivine/plagioclase ratios depending on the environmental conditions. CF values are closer to a linear mixing relationship for <50% plagioclase under ambient conditions and >50% plagioclase under lunar-like conditions.

Nonlinear spectral mixing also occurs at wavelengths other than the CF region. Changes in overall emissivity with mixture composition differ between the two environments. In ambient conditions, the emissivity at most wavelengths decreases as the amount of olivine in the mixture increases, while under lunar conditions, all of the mixtures have higher emissivity than the 100% plagioclase sample, and there are many regions in the spectrum where the mixtures have a higher apparent emissivity than either of the pure minerals. This trend for emissivity is not expected regardless of whether modeled linearly mixed spectra are normalized to a maximum emissivity of one. The behavior under lunar conditions could be due to the high albedo of pure anorthite, which makes it difficult to reach the desired sample temperature, thus affecting the acquired emissivity spectrum. Additionally, while laboratory data show a consistent trend in our concavity-based olivine index with composition, the overall emissivity values do not directly correlate with olivine abundance in the 13–23 μm region.

4.2. The Impact of Olivine Composition on Abundance Constraints

The Fo# affects the inferred olivine abundance as the wavelength of CF position increases with Fe content (SOM) [Greenhagen *et al.*, 2010]. The presence of Fe-rich olivine would substantially lower our MIR-based estimated olivine abundance estimates. The possibility of fayalitic olivine at olivine-enriched locations also presents a problem for VNIR models that predict these areas to have a “dunite” composition [Yamamoto *et al.*, 2010], as these models are based on a composition of Fo₉₀. However, only one region included in this study, a small crater within the Nectaris basin, stands out based on its high CF position and spectral shape, both of which could be due to the presence of fayalitic olivine. Furthermore, Corley *et al.* [2014] infer an Fe-rich composition for olivine at this site based on M³ data, making it likely of a basaltic origin, and hence not representative of most olivine-rich, pyroxene poor locations on the Moon. Interestingly, this is one of a few sites that occur within a basin, rather than on the outskirts. According to Corley *et al.* [2014], data from the Gravity Recovery and Interior Laboratory mission show that it is unlikely this impact crater reached the crust/mantle boundary.

4.3. Interpretation of Estimated Plagioclase-Olivine Ratios

When interpreting the Diviner CF data, we assume that our compositional estimates are not substantially altered by presence of agglutinate glass. The formation of agglutinate glass from crystalline material

influences effective emissivity spectra through two processes: (1) a change in particle size distribution and (2) vitrification. Although agglutination produces larger grains as measured by a sieve, they are irregularly shaped and porous, likely acting as several smaller scatterers [Nash *et al.*, 1993]. Vitrification removes absorptions due to lattice vibrations, reducing the number of features in the spectrum down to a set of simple molecular vibrations. This removes many of the reststrahlen band features and shifts some of the bands to different wavelengths. However, Nash and Salisbury [1991] found that the position of the CF did not change between crystalline plagioclase and plagioclase glass of the same calcium content. Olivine is less amenable to shock than plagioclase. Koizumi *et al.* [2010] show that unlike plagioclase, olivine still shows a typical MIR spectrum under shock pressures of up to 40 GPa. Hence, the CF position is expected to remain constant with chemical composition, regardless of the state of crystallinity. Additionally, since the agglutination process is part of space weathering, this should be accounted for in the OMAT correction.

We find that olivine-bearing locations display a wide range of olivine/plagioclase ratios, most of which are comparable to abundances found in troctolite (10–60% plagioclase, 40–90% olivine, and less than 10% pyroxene) [Stoffler *et al.*, 1980]. Possible mechanisms for the occurrence of compositions resembling these rock types at the lunar surface include (1) direct exposure of the olivine-rich lunar mantle through impact processes which have likely mechanically mixed the crust through subsequent impacts, (2) impact exposure of olivine-rich lunar mantle that has experienced melting and interaction with the crust, or (3) intrusion of olivine-rich plutons into the crust that have been excavated by impacts.

Yamamoto *et al.* [2012] favor the second option and suggest a sequence of events that could bring olivine-bearing, upper mantle material to the lunar surface: (1) some basin-forming impacts were large enough to melt material from the crust and upper mantle [e.g., Stewart, 2011], (2) differentiated melt sheets were produced with olivine-rich materials at the bottom [Vaughan *et al.*, 2013], and (3) subsequent impacts excavated material from the lower layers of the melt sheet, exposing them at the surface. This model would explain the patchy distribution of these olivine-enriched sites.

Impact simulations by Miljković *et al.* [2015] support the idea that several of the larger lunar impact basins should have excavated upper mantle, most prominently Crisium on the nearside and Moscoviense on the far side. Since the centers of these basins have been subsequently infilled with mare basalts, the exposures that remain visible are expected to lie just outside the mare basalts. These results are generally in agreement with the locations of olivine-rich areas identified from orbital data, with the notable exception of the lack of observed olivine in the vicinity of Mare Smythii. As pointed out in Miljković *et al.* [2015], Smythii is one of the oldest lunar basins; hence, any mantle exposures may have covered by ejecta of later impacts. Whether mantle remains at the surface is likely a function of both the impact conditions (preimpact crustal thickness, impactor size) and the basin formation age.

An additional constraint on olivine detection in the VNIR is that olivine-bearing surfaces must be relatively fresh, or the 1 μm band will be diminished by space weathering processes. Yamamoto *et al.* [2012] suggest that this is another possible reason for the heterogeneous distribution of VNIR olivine detections, as fresh sites are relatively rare. However, Diviner should be uniquely sensitive to very high olivine abundances, even, or especially, in the presence of space weathering. Olivine shows the longest CF value of the major lunar minerals, and space weathering drives the CF value to even longer wavelengths [Greenhagen *et al.*, 2010]. Based on ambient laboratory reflectance measurements of lunar soils, this effect was not expected as previous experiments showed that CF position has a linear relationship to composition irrespective of exposure age [Nash *et al.*, 1993; Salisbury *et al.*, 1997; Lucey *et al.*, 2016]. A global search of the Diviner and M³ data sets has not revealed extensive exposures of material with long CF values, but weak or absent 1 μm absorption in the VNIR [Greenhagen *et al.*, 2010], suggesting that mature, nearly pure olivine is not present on the lunar surface at spatial scales resolvable by Diviner (500–1000 m). Moreover, a wide range of OMAT values is observed at olivine-bearing sites (Table 1b), suggesting that optical maturity does not appreciably affect the observed distribution of olivine on the lunar surface.

After direct and processed upper mantle exposures, another possible mechanism is that the olivine-bearing regions originate from Mg-suite plutons that were excavated by impacts. A large number of models for the both the formation of the Mg-suite and the troctolites, in particular, have been proposed [Griffiths and Campbell, 1990; Ryder, 1991; Hess, 1994, 1998, 2000; Ryder *et al.*, 1997; Longhi, 2003; Shearer and Papike, 2005].

The main difficulty that has led to the profusion of models is the incorporation of a potassium, rare earth element, and phosphorus-like concentration of incompatible elements while retaining a high Mg/Fe ratio. A hybrid source model for Mg-rich magmas such as the one suggested by *Elardo et al.* [2011] is another possibility.

Hess [1994] reviews the problems with the Mg-suite formation models that had been proposed to date and considers an impact origin as an alternative, following *Grieve et al.* [1991], who argue that the Sudbury Igneous Complex is a differentiated impact melt sheet and may be an analog for lunar impact structures. For lunar troctolite, *Hess* [1994] does not favor the impact scenario because it would not explain the gap in An# versus Mg# trends between the ferroan anorthositic (FAN) suite and the Mg-suite that had been observed in Apollo samples up to that point. There are clasts from highlands breccias that fall within this range [*Lindstrom and Lindstrom*, 1986], and as more lunar meteorite samples have been recovered, this gap has closed [*Takeda et al.*, 1990, 2006]. However, these samples may not be geochemically related to either FAN- or Mg-suite rocks [*Korotev et al.*, 2003]. It is possible then that there are at least two common lunar lithologies with similar olivine/plagioclase ratios.

In summary, it is difficult to distinguish between (1) the crystallized product of an impact-generated melt that chemically mixed upper mantle with crust and (2) preexisting troctolite and/or dunite plutons that were exposed and have likely mechanically mixed with the anorthositic crust, during or postimpact. Complicating things further is the possibility that troctolites *are the result of the former*, rather than magmatic processes [*Grieve et al.*, 1991; *Hess*, 1994; *Lucey*, 2010]. In either case we would expect these sites to have a wide distribution of olivine/plagioclase ratios. However, assuming a Fo₉₀ olivine composition, we find that the distribution of olivine abundances is centered around 50–60 wt % (45–55 vol %) olivine, with four sites in the range of 70–90 wt % (66–85 vol %). The range of olivine abundances in lunar troctolite is approximately 30–70 vol % [*Kaula et al.*, 1981]. Given the upper bound of 70 vol % olivine in lunar troctolite, it seems improbable that an impact-generated mixture of preexisting troctolite with anorthositic crust would produce the olivine abundances on the higher end of the observed distribution.

5. Conclusions

Using MIR Diviner data along with lunar-like environment effective emissivity measurements, we have placed constraints on olivine abundance within olivine-bearing, pyroxene-poor regions detected by VNIR instruments. Laboratory spectra show that at the small grain sizes typical of lunar regolith, MIR spectra do not combine linearly. This nonlinearity affects compositional estimates inferred from the CF position. We then applied the lunar environment laboratory data of mineral mixtures to Diviner remote sensing data, assuming a two-component olivine-plagioclase mixture. To aid identification of olivine enrichment using the Diviner data set, we developed a spectral index using one of Diviner's "thermal" channels (Ch 6, covering ~13–23 μm).

We have accounted for the effects of space weathering by applying an OMAT correction to the Diviner CF values. While analysis of VNIR data requires a fresh surface to detect olivine exposures, MIR data of space-weathered olivine would actually lead to an overestimate of olivine abundance without correction. Since high-CF areas not correlated with VNIR olivine detections have not been observed, the sporadic distribution of olivine-enriched areas likely is the unbiased distribution of troctolitic material exposed at the lunar surface at the scale of Diviner spatial resolution (250 m). The olivine abundance estimates presented here would decrease relative to plagioclase for locations featuring more fayalitic olivine than that used in our laboratory measurements.

Of the 30 locations investigated, none are unambiguously consistent with dunite (>90 wt % olivine) even assuming a high Fo# (Fo₉₁). These areas display a wide distribution of estimated upper limits for olivine weight percentages, ranging from 12% to 87%. This is in contrast to estimates derived from VNIR data that place some of these regions at >90% olivine. Our abundance estimates include four locations that are between 71 and 87 wt % olivine, which within methodological uncertainties could be consistent with dunite. The upper bound we give for these locations ranges from 84 to 97 wt % olivine. These estimates do not exclude an upper mantle-derived (even if indirect) origin for olivine in these regions, as mixture with a significant amount of crustal material would be expected either through exposure of the lower portions of a differentiated melt sheet or overprinting with ejecta of later impacts.

Acknowledgments

We would like to thank Sara Russell for collecting anorthite microprobe measurements. Funding support for J.A.A., T.D.G., P.G.L., E.S., and B.T.G. was provided by the Diviner Lunar Radiometer Extended Mission science investigation (D.A. Paige Principal Investigator) and the RIS⁴E Solar System Exploration Research Virtual Institute investigation (T.D.G. Principal Investigator). We would also like to thank Leah Cheek and an anonymous reviewer for their thorough examination of the manuscript and suggestions for improvement. This is SSERVI publication number SSERVI-2015-127. Diviner and M³ data products can be accessed via the PDS Geosciences Node Lunar Orbital Data Explorer (<http://ode.rsl.wustl.edu/moon/>). SELENE (Kaguya) data products are available at <http://l2db.selene.darts.isas.jaxa.jp/index.html.en>. Emissivity spectra collected in support of this work will be archived at <http://aram.ess.sunysb.edu/spectra.html> following acceptance of this publication.

References

- Adams, J. B., and L. H. Goulaud (1978), Plagioclase feldspars—Visible and near infrared diffuse reflectance spectra as applied to remote sensing, *Lunar Planet. Sci. Conf. Proc.*, *9*, 2901–2909.
- Adams, J. B., and T. B. McCord (1972), Electronic spectra of pyroxenes and interpretation of telescopic spectral reflectivity curves of the Moon, *Lunar Planet. Sci. Conf. Proc.*, *3*, 3021.
- Adams, J. B., F. Horz, and R. V. Gibbons (1979), Effects of shock-loading on the reflectance spectra of plagioclase, pyroxene, and glass, *Lunar Planet. Sci. Conf. Proc.*, *10*, 1–3.
- Adams, J. B., M. O. Smith, and P. E. Johnson (1986), Spectral mixture modeling: A new analysis of rock and soil types at the Viking Lander 1 site, *J. Geophys. Res.*, *91*(B8), 8098–8112, doi:10.1029/JB091iB08p08098.
- Aronson, J. R., and A. G. Emslie (1973), Spectral reflectance and emittance of particulate materials. 2: Application and results, *Appl. Opt.*, *12*(11), 2573–2584, doi:10.1364/AO.12.002573.
- Bandfield, J. L., P. O. Hayne, J.-P. Williams, B. T. Greenhagen, and D. A. Paige (2015), Lunar surface roughness derived from LRO Diviner Radiometer observations, *Icarus*, *248*, 357–372, doi:10.1016/j.icarus.2014.11.009.
- Boardman, J. W., C. M. Pieters, R. O. Green, S. R. Lundeen, P. Varanasi, J. Nettles, N. Petro, P. Isaacson, S. Besse, and L. A. Taylor (2011), Measuring moonlight: An overview of the spatial properties, lunar coverage, selenolocation, and related Level 1B products of the Moon Mineralogy Mapper, *J. Geophys. Res.*, *116*, E00G14, doi:10.1029/2010JE003730.
- Cahill, J. T. S., P. G. Lucey, K. R. Stockstill-Cahill, and B. R. Hawke (2010), Radiative transfer modeling of near-infrared reflectance of lunar highland and mare soils, *J. Geophys. Res.*, *115*, E12013, doi:10.1029/2009JE003500.
- Cheek, L. C., and C. M. Pieters (2014), Reflectance spectroscopy of plagioclase-dominated mineral mixtures: Implications for characterizing lunar anorthosites remotely, *Am. Mineral.*, *99*(10), 1871–1892.
- Conel, J. E. (1969), Infrared emissivities of silicates: Experimental results and a cloudy atmosphere model of Spectral emission from condensed particulate mediums, *J. Geophys. Res.*, *74*(6), 1614–1634, doi:10.1029/JB074i006p01614.
- Corley, L. M., P. J. McGovern, and G. Y. Kramer (2014), Olivine exposures on the Moon: Origins and mechanisms of transport to the lunar surface, *Lunar and Planetary Institute Science Conference Abstracts*, vol. 45, p. 1564.
- Crown, D. A., and C. M. Pieters (1987), Spectral properties of plagioclase and pyroxene mixtures and the interpretation of lunar soil spectra, *Icarus*, *72*(3), 492–506.
- Denevi, B. W., P. G. Lucey, and S. B. Sherman (2008), Radiative transfer modeling of near-infrared spectra of lunar mare soils: Theory and measurement, *J. Geophys. Res.*, *113*, E02003, doi:10.1029/2007JE002929.
- Dhingra, D., C. M. Pieters, J. W. Boardman, J. W. Head, P. J. Isaacson, and L. A. Taylor (2011), Compositional diversity at Theophilus Crater: Understanding the geological context of Mg-spinel bearing central peaks, *Geophys. Res. Lett.*, *38*, L11201, doi:10.1029/2011GL047314.
- Donaldson Hanna, K. L., M. B. Wyatt, I. R. Thomas, N. E. Bowles, B. T. Greenhagen, A. Maturilli, J. Helbert, and D. A. Paige (2012a), Thermal infrared emissivity measurements under a simulated lunar environment: Application to the Diviner Lunar Radiometer Experiment, *J. Geophys. Res.*, *117*, E00H05, doi:10.1029/2011JE003862.
- Donaldson Hanna, K. L., I. R. Thomas, N. E. Bowles, B. T. Greenhagen, C. M. Pieters, J. F. Mustard, C. R. M. Jackson, and M. B. Wyatt (2012b), Laboratory emissivity measurements of the plagioclase solid solution series under varying environmental conditions, *J. Geophys. Res.*, *117*, E11004, doi:10.1029/2012JE004184.
- Donaldson Hanna, K. L., I. R. Thomas, B. T. Greenhagen, N. E. Bowles, and C. M. Pieters (2014a), Characterization of Apollo soil samples under simulated lunar conditions, *Lunar and Planetary Institute Science Conference Abstracts*, vol. 45, p. 2345.
- Donaldson Hanna, K. L., L. C. Cheek, C. M. Pieters, J. F. Mustard, B. T. Greenhagen, I. R. Thomas, and N. E. Bowles (2014b), Global assessment of pure crystalline plagioclase across the Moon and implications for the evolution of the primary crust, *J. Geophys. Res. Planets*, *119*, 1516–1545, doi:10.1002/2013JE004476.
- Dyar, M. D., E. C. Sklute, O. N. Menzies, P. A. Bland, D. Lindsley, T. Glotch, M. D. Lane, M. W. Schaefer, B. Wopenka, and R. Klima (2009), Spectroscopic characteristics of synthetic olivine: An integrated multi-wavelength and multi-technique approach, *Am. Mineral.*, *94*(7), 883–898.
- Elardo, S. M., D. S. Draper, and C. K. Shearer Jr. (2011), Lunar Magma Ocean crystallization revisited: Bulk composition, early cumulate mineralogy, and the source regions of the highlands Mg-suite, *Geochim. Cosmochim. Acta*, *75*(11), 3024–3045.
- Glotch, T. D., et al. (2010), Highly silicic compositions on the Moon, *Science*, *329*(5998), 1510–1513, doi:10.1126/science.1192148.
- Glotch, T. D., J. J. Hagerty, P. G. Lucey, B. Hawke, T. A. Giguere, J. A. Arnold, J. Williams, B. L. Jolliff, and D. A. Paige (2011), The Marian domes: Silicic volcanic constructs on the Moon, *Geophys. Res. Lett.*, *38*, L21204, doi:10.1029/2011GL049548.
- Glotch, T. D., J. L. Bandfield, P. G. Lucey, P. O. Hayne, B. T. Greenhagen, J. A. Arnold, R. R. Ghent, and D. A. Paige (2015), Formation of lunar swirls by magnetic field standoff of the solar wind, *Nat. Commun.*, *6*.
- Goswami, J. N., and M. Annadurai (2008), Chandrayaan-1 mission to the Moon, *Acta Astronaut.*, *63*(11), 1215–1220.
- Greenhagen, B. T., et al. (2010), Global silicate mineralogy of the Moon from the Diviner Lunar Radiometer, *Science*, *329*(5998), 1507–1509, doi:10.1126/science.1192196.
- Greenhagen, B. T., P. G. Lucey, J. L. Bandfield, P. O. Hayne, J. P. Williams, and D. A. Paige (2011), The Diviner Lunar Radiometer compositional data products: Description and examples, *Lunar and Planetary Institute Science Conference Abstracts*, vol. 42, p. 2679.
- Grieve, R. A. F., D. Stoffer, and A. Deutsch (1991), The Sudbury structure—Controversial or misunderstood?, *J. Geophys. Res.*, *96*(E5), 22,753–22,764, doi:10.1029/91JE02513.
- Griffiths, R. W., and I. H. Campbell (1990), Stirring and structure in mantle starting plumes, *Earth Planet. Sci. Lett.*, *99*(1–2), 66–78, doi:10.1016/0012-821X(90)90071-5.
- Hamilton, V. E. (2010), Thermal infrared (vibrational) spectroscopy of Mg–Fe olivines: A review and applications to determining the composition of planetary surfaces, *Icarus*, *70*, 7–33, doi:10.1016/j.icarus.2009.12.005.
- Hapke, B. (1981), Bidirectional reflectance spectroscopy: 1. Theory, *J. Geophys. Res.*, *86*(B4), 3039–3054, doi:10.1029/JB086iB04p03039.
- Hapke, B. (1993), *Introduction to the Theory of Reflectance and Emission Spectroscopy*, 1st ed., Cambridge Univ. Press, New York.
- Heiken, G. H., D. T. Vaniman, and B. M. French (1991), *Lunar Sourcebook—A User's Guide to the Moon*, Cambridge Univ. Press, Cambridge, U. K.
- Henderson, B. G., and B. M. Jakosky (1994), Near-surface thermal gradients and their effects on mid-infrared emission spectra of planetary surfaces, *J. Geophys. Res.*, *99*(E9), 19,063–19,073, doi:10.1029/94JE01861.
- Hess, P. C. (1994), Petrogenesis of lunar troctolites, *J. Geophys. Res.*, *99*(E9), 19,083–19,093, doi:10.1029/94JE01868.
- Hess, P. C. (1998), Source regions to lunar troctolite parent magmas, *Lunar and Planetary Institute Science Conference Abstracts*, vol. 29, p. 1225.
- Hess, P. C. (2000), Petrogenesis of lunar troctolites—Implications for the Moon and its evolution, *Lunar and Planetary Institute Science Conference Abstracts*, vol. 31, p. 1389.

- Isaacson, P. J., et al. (2011), Remote compositional analysis of lunar olivine-rich lithologies with Moon Mineralogy Mapper (M^3) spectra, *J. Geophys. Res.*, *116*, E00G11, doi:10.1029/2010JE003731.
- Isaacson, P. J., R. L. Klima, J. M. Sunshine, L. C. Cheek, C. M. Pieters, T. Hiroi, M. D. Dyar, M. Lane, and J. Bishop (2014), Visible to near-infrared optical properties of pure synthetic olivine across the olivine solid solution, *Am. Mineral.*, *99*(2–3), 467–478.
- Johnson, J. R., and F. Hörz (2003), Visible/near-infrared spectra of experimentally shocked plagioclase feldspars, *J. Geophys. Res.*, *108*(E11), 5120, doi:10.1029/2003JE002127.
- Kato, M., S. Sasaki, K. Tanaka, Y. Iijima, and Y. Takizawa (2008), The Japanese lunar mission SELENE: Science goals and present status, *Adv. Space Res.*, *42*(2), 294–300, doi:10.1016/j.asr.2007.03.049.
- Kaula, W. M., J. W. Head III, R. B. Merrill, R. O. Pepin, S. C. Solomon, D. Walker, and C. A. Wood (1981), Basaltic volcanism on the terrestrial planets, in *Basaltic volcanism Terr. planets*, edited by W. M. Kaula et al., pp. 1286, Pergamon Press, Oxford-New York-Frankfurt-Paris-Sydney-Toronto-Tokyo.
- Klima, R. L., C. M. Pieters, and M. D. Dyar (2008), Characterization of the 1.2 μm $M1$ pyroxene band: Extracting cooling history from near-IR spectra of pyroxenes and pyroxene-dominated rocks, *Meteorit. Planet. Sci.*, *43*(10), 1591–1604, doi:10.1111/j.1945-5100.2008.tb00631.x.
- Klima, R. L., C. M. Pieters, J. W. Boardman, R. O. Green, J. W. Head, P. J. Isaacson, J. F. Mustard, J. W. Nettles, N. E. Petro, and M. I. Staid (2011), New insights into lunar petrology: Distribution and composition of prominent low-Ca pyroxene exposures as observed by the Moon Mineralogy Mapper (M^3), *J. Geophys. Res.*, *116*, E00G06, doi:10.1029/2010JE003719.
- Koizumi, E., T. Mikouchi, A. Monkawa, T. Kurihara, and M. Miyamoto (2010), Micro FTIR analysis of brown olivines in Martian meteorites, *Lunar and Planetary Institute Science Conference Abstracts*, vol. 41, 1575.
- Korotev, R. L., B. L. Jolliff, R. A. Zeigler, J. J. Gillis, and L. A. Haskin (2003), Feldspathic lunar meteorites and their implications for compositional remote sensing of the lunar surface and the composition of the lunar crust, *Geochim. Cosmochim. Acta.*, *67*(24), 4895–4923.
- Kramer, G. Y., D. A. Kring, A. L. Nahm, and C. M. Pieters (2013), Spectral and photogeologic mapping of Schrödinger Basin and implications for post-South Pole-Aitken impact deep subsurface stratigraphy, *Icarus*, *223*(1), 131–148.
- Lindstrom, M. M., and D. J. Lindstrom (1986), Lunar granulites and their precursor anorthositic norites of the early lunar crust, *J. Geophys. Res.*, *91*(B4), 263–276, doi:10.1029/JB091iB04p0D263.
- Logan, L. M., G. R. Hunt, J. W. Salisbury, and S. R. Balsamo (1973), Compositional implications of Christiansen frequency maximums for infrared remote sensing applications, *J. Geophys. Res.*, *78*(23), 4983–5003, doi:10.1029/JB078i023p04983.
- Longhi, J. (2003), A new view of lunar ferroan anorthosites: Postmagma ocean petrogenesis, *J. Geophys. Res.*, *108*(E8), 5083, doi:10.1029/2002JE001941.
- Lucey, P. G. (2010), Planetary science: Mantle of the Moon exposed?, *Nat. Geosci.*, *3*(8), 517–518.
- Lucey, P. G., B. R. Hawke, C. M. Pieters, J. W. Head, and T. B. McCord (1986), A compositional study of the Aristarchus Region of the Moon using near-infrared reflectance spectroscopy, *J. Geophys. Res.*, *91*(B4), 344–354, doi:10.1029/JB091iB04p0D344.
- Lucey, P. G., B. R. Hawke, and K. Horton (1991), The distribution of olivine in the Crater Copernicus, *Geophys. Res. Lett.*, *18*(11), 2133–2136, doi:10.1029/91GL02538.
- Lucey, P. G., D. T. Blewett, G. J. Taylor, and B. R. Hawke (2000), Imaging of lunar surface maturity, *J. Geophys. Res.*, *105*(E8), 20,377–20,386, doi:10.1029/1999JE001110.
- Lucey, P. G., D. A. Paige, B. T. Greenhagen, J. L. Bandfield, and T. D. Glotch (2010), Comparison of Diviner Christiansen Feature position and visible albedo: Composition and space weathering implications, *Lunar and Planetary Institute Science Conference Abstracts*, vol. 41, p. 1600.
- Lucey, P. G., et al. (2016), Space weathering effects in Diviner Lunar Radiometer multispectral infrared measurements of the lunar Christiansen Features: Characteristics and mitigation, *Icarus*, doi:10.1016/j.icarus.2016.05.010, in press.
- Lundeen, S. (2011), Chandrayaan-1 Moon Mineralogy Mapper calibration data record, CH1-ORB-L-M3-4-L1B-RADIANCE-V3.0, NASA Planetary Data System.
- Lyon, R. J. P. (1964), Evaluation of infrared spectrophotometry for compositional analysis of lunar and planetary soils: Rough and powdered surfaces, part 2, final report, contract NASR 49 (04).
- Miljković, K., M. A. Wieczorek, G. S. Collins, S. C. Solomon, D. E. Smith, and M. T. Zuber (2015), Excavation of the lunar mantle by basin-forming events on the Moon, *Earth Planet. Sci. Lett.*, *409*, 243–251.
- Mustard, J. F., et al. (2011), Compositional diversity and geologic insights of the Aristarchus crater from Moon Mineralogy Mapper data, *J. Geophys. Res.*, *116*, E00G12, doi:10.1029/2010JE003726.
- Nash, D. B., and J. E. Conel (1974), Spectral reflectance systematics for mixtures of powdered hypersthene, labradorite, and ilmenite, *J. Geophys. Res.*, *79*(11), 1615–1621, doi:10.1029/JB079i011p01615.
- Nash, D. B., and J. W. Salisbury (1991), Infrared reflectance spectra (2.2–15 μm) of plagioclase feldspars, *Geophys. Res. Lett.*, *18*(6), 1151–1154, doi:10.1029/91GL01008.
- Nash, D. B., J. W. Salisbury, J. E. Conel, P. G. Lucey, and P. R. Christensen (1993), Evaluation of infrared emission spectroscopy for mapping the moon's surface composition from lunar orbit, *J. Geophys. Res.*, *98*(E12), 23,535–23,552, doi:10.1029/93JE02604.
- Noble, S. K., C. M. Pieters, L. A. Taylor, R. V. Morris, C. C. Allen, D. S. McKay, and L. P. Keller (2000), The optical properties of the finest fraction of lunar soil: Implications for space weathering, *Meteorit. Planet. Sci.*, *36*, 31–42.
- Ohtake, M., T. Matsunaga, J. Haruyama, Y. Yokota, T. Morota, C. Honda, Y. Ogawa, M. Torii, H. Miyamoto, and T. Arai (2009), The global distribution of pure anorthosite on the Moon, *Nature*, *461*(7261), 236–240.
- Paige, D. A., et al. (2010), The Lunar Reconnaissance Orbiter Diviner Lunar Radiometer Experiment, *Space Sci. Rev.*, *150*(1–4), 125–160, doi:10.1007/s11214-009-9529-2.
- Pan, C., and A. D. Rogers (2014), Thermal infrared spectral analysis of fine grained compacted mineral mixtures: assessment of applicability of Partial Least Squares (PLS) methods and implications for spectral interpretations of Martian sedimentary materials, *Lunar and Planetary Science Conference Abstracts*, vol. 45, Abstract 2228.
- Papike, J., L. Taylor, and S. Simon (1991), Lunar minerals, in *Lunar Sourcebook*, pp. 121–181, Cambridge Univ. Press, Cambridge, U. K.
- Pieters, C. M. (1982), Copernicus crater central peak: Lunar mountain of unique composition, *Science*, *215*(4528), 59–61, doi:10.1126/science.215.4528.59.
- Pieters, C. M. (1996), Plagioclase and maskelynite diagnostic features, *Lunar and Planetary Institute Science Conference Abstracts*, vol. 27, p. 1031.
- Pieters, C. M., et al. (2009), The Moon Mineralogy Mapper (M^3) on Chandrayaan-1, *Curr. Sci.*, *96*(4), 500–505.
- Powell, K. E., P. J. McGovern, and G. Y. Kramer (2012), Olivine detections at the rim of Crisium Basin with Moon Mineralogy Mapper, *Lunar and Planetary Institute Science Conference Abstracts*, vol. 43, p. 1689.
- Ramsey, M. S., and P. R. Christensen (1998), Mineral abundance determination: Quantitative deconvolution of thermal emission spectra, *J. Geophys. Res.*, *103*(B1), 577–596, doi:10.1029/97JB02784.
- Ruff, S. W., and P. R. Christensen (2002), Bright and dark regions on Mars: Particle size and mineralogical characteristics based on Thermal Emission Spectrometer data, *J. Geophys. Res.*, *107*(E12), 5119, doi:10.1029/2001JE001580.

- Ruff, S. W., P. R. Christensen, P. W. Barbera, and D. L. Anderson (1997), Quantitative thermal emission spectroscopy of minerals: A laboratory technique for measurement and calibration, *J. Geophys. Res.*, *102*(B7), 14,899–14,913, doi:10.1029/97JB00593.
- Ryder, G. (1991), Lunar ferroan anorthosites and mare basalt sources—The mixed connection, *Geophys. Res. Lett.*, *18*(11), 2065–2068, doi:10.1029/91GL02535.
- Ryder, G., M. D. Norman, and G. J. Taylor (1997), The complex stratigraphy of the highland crust in the Serenitatis region of the Moon inferred from mineral fragment chemistry, *Geochim. Cosmochim. Acta*, *61*(5), 1083–1105, doi:10.1016/S0016-7037(96)00386-9.
- Salisbury, J. W., and A. Wald (1992), The role of volume scattering in reducing spectral contrast of reststrahlen bands in spectra of powdered minerals, *Icarus*, *96*(1), 121–128.
- Salisbury, J. W., and L. S. Walter (1989), Thermal infrared (2.5–13.5 μm) spectroscopic remote sensing of igneous rock types on particulate planetary surfaces, *J. Geophys. Res.*, *94*(B7), 9192–9202, doi:10.1029/JB094iB07p09192.
- Salisbury, J. W., B. Hapke, and J. W. Eastes (1987), Usefulness of weak bands in midinfrared remote sensing of particulate planetary surfaces, *J. Geophys. Res.*, *92*(B1), 702–710, doi:10.1029/JB092iB01p00702.
- Salisbury, J. W., A. Basu, and E. M. Fischer (1997), Thermal infrared spectra of lunar soils, *Icarus*, *130*(1), 125–139, doi:10.1006/icar.1997.5809.
- Serventi, G., C. Carli, M. Sgavetti, M. Ciarniello, F. Capaccioni, and G. Pedrazzi (2013), Spectral variability of plagioclase–mafic mixtures (1): Effects of chemistry and modal abundance in reflectance spectra of rocks and mineral mixtures, *Icarus*, *226*(1), 282–298.
- Shearer, C. K., and J. J. Papike (2005), Early crustal building processes on the moon: Models for the petrogenesis of the magnesian suite, *Geochim. Cosmochim. Acta*, *69*(13), 3445–3461.
- Shirley, K. A., and T. D. Glotch (2014), A correction to the thermal bands for the Diviner Lunar Radiometer Experiment, *Lunar and Planetary Institute Science Conference Abstracts*, vol. 45, p. 2399.
- Shirley, K. A., and T. D. Glotch (2015), First measurements from the Planetary and Asteroid Regolith Spectroscopy Environmental Chamber (PARSEC), *Lunar and Planetary Science Conference Abstracts*, vol. 46, p. 2025.
- Shkuratov, Y., L. Starukhina, H. Hoffmann, and G. Arnold (1999), A model of spectral albedo of particulate surfaces: Implications for optical properties of the Moon, *Icarus*, *137*(2), 235–246, doi:10.1006/icar.1998.6035.
- Starukhina, L. V., Y. G. Shkuratov, O. D. Rode, and C. M. Pieters (1994), Reflectance spectra of particle size separates of lunar soils: Is the difference controlled by reduced iron?, *LPS XXV*, 1333.
- Stewart, S. T. (2011), Impact basin formation: The mantle excavation paradox resolved, *Lunar and Planetary Institute Science Conference Abstracts*, vol. 42, p. 1633.
- Stoffler, D., H. D. Knollz, U. B. Marving, and C. H. Simonds (1980), Lunar highland rocks—A committee report, *Proc. Conf. Lunar Highlands Crust*, pp. 51–70.
- Sunshine, J. M., and C. M. Pieters (1998), Determining the composition of olivine from reflectance spectroscopy, *J. Geophys. Res.*, *103*(E6), 13,675–13,688, doi:10.1029/98JE01217.
- Sunshine, J. M., C. M. Pieters, and S. F. Pratt (1990), Deconvolution of mineral absorption bands: An improved approach, *J. Geophys. Res.*, *95*(B5), 6955–6966, doi:10.1029/JB095iB05p06955.
- Takeda, H., M. Miyamoto, H. Mori, S. J. Wentworth, and D. S. McKay (1990), Mineralogical comparison of the Y86032-type lunar meteorites to feldspathic fragmental breccia 67016, *Lunar Planet. Sci. Conf. Proc.*, *20*, 91–100.
- Takeda, H., A. Yamaguchi, D. D. Bogard, Y. Karouji, M. Ebihara, M. Ohtake, K. Saiki, and T. Arai (2006), Magnesian anorthosites and a deep crustal rock from the farside crust of the moon, *Earth Planet. Sci. Lett.*, *247*(3–4), 171–184, doi:10.1016/j.epsl.2006.04.004.
- Thomas, I. R., N. E. Bowles, B. T. Greenhagen, T. D. Glotch, K. L. Donaldson Hanna, M. B. Wyatt, J. L. Bandfield, and D. A. Paige (2010), Emission measurements of lunar analogues for interpretation of returning data from the Diviner Lunar Radiometer on NASA's Lunar Reconnaissance Orbiter, *Lunar and Planetary Institute Science Conference Abstracts*, vol. 41, p. 1364.
- Thomas, I. R., B. T. Greenhagen, N. E. Bowles, K. L. Donaldson Hanna, J. Temple, and S. B. Calcutt (2012), A new experimental setup for making thermal emission measurements in a simulated lunar environment, *Rev. Sci. Instrum.*, *83*(12), 124502, doi:10.1063/1.4769084.
- Thomson, J. L., and J. W. Salisbury (1993), The mid-infrared reflectance of mineral mixtures (7–14 μm), *Remote Sens. Environ.*, *45*(1), 1–13.
- Tompkins, S., and C. M. Pieters (1999), Mineralogy of the lunar crust: Results from Clementine, *Meteorit. Planet. Sci.*, *34*(1), 25–41, doi:10.1111/j.1945-5100.1999.tb01729.x.
- Vaughan, W. M., J. W. Head, L. Wilson, and P. C. Hess (2013), Geology and petrology of enormous volumes of impact melt on the Moon: A case study of the Orientale basin impact melt sea, *Icarus*, *223*(2), 749–765, doi:10.1016/j.icarus.2013.01.017.
- Warren, P. H. (1993), A concise compilation of petrologic information on possibly pristine nonmare Moon rocks, *Am. Mineral.*, *78*, 360–376.
- Wieczorek, M. A., B. L. Jolliff, A. Khan, M. E. Pritchard, B. P. Weiss, J. D. Williams, L. L. Hood, K. Righter, C. R. Neal, and C. K. Shearer (2006), New views of the moon, *Rev. Min. Geochem.*, *60*, 221–364.
- Yamamoto, S., et al. (2010), Possible mantle origin of olivine around lunar impact basins detected by SELENE, *Nat. Geosci.*, *3*(8), 533–536, doi:10.1038/ngeo897.
- Yamamoto, S., et al. (2012), Olivine-rich exposures in the South Pole-Aitken Basin, *Icarus*, *218*(1), 331–344, doi:10.1016/j.icarus.2011.12.012.